General-relativistic force-free pulsar magnetospheres

J. Pétri

General-relativistic force-free pulsar magnetospheres

J. Pétri[★]

Observatoire astronomique de Strasbourg, Université de Strasbourg, CNRS, UMR 7550, 11 rue de l'université, F-67000 Strasbourg, France

ABSTRACT

Pulsar magnetospheres are shaped by ultrarelativistic electron/positron plasmas flowing in a strong magnetic field and subject to strong gravitational fields. The former induces magnetospheric currents and space charges responsible for the distortion of the electromagnetic field based on pure electrodynamics. The latter induces other perturbations in these fields based on space–time curvature. The force-free approximation describes the response of this magnetosphere to the presence of currents and charges and has been investigated by many authors. In this context, general relativity has been less discussed to quantify its influence on the neutron star electrodynamics. It is the purpose of this paper to compute general-relativistic force-free pulsar magnetospheres for realistic magnetic field configurations such as the inclined dipole. We performed time-dependent simulations of Maxwell equations in the 3+1 formalism of a stationary background metric in the slow-rotation approximation. We computed the resulting Poynting flux depending on the ratio R/r_L and on frame-dragging through the spin parameter a_s, R is the neutron star radius and r_L the light-cylinder radius. Both effects act together to increase the total Poynting flux seen by a distant observer by a factor up to 2 depending on the rotation rate. Moreover we retrieve the $\sin^2\chi$ dependence of this luminosity, χ being the obliquity of the pulsar, as well as a braking index close to $n = 3$. We also show that the angular dependence of the Poynting flux scales like $\sin^2\vartheta$ for the aligned rotator but like $\sin^4\vartheta$ for the orthogonal rotator, ϑ being the colatitude.

Key words: gravitation – magnetic fields – plasmas – methods: analytical – methods: numerical – stars: neutron.

1 INTRODUCTION

Neutron stars are places where strongly magnetized and relativistic plasmas are embedded in a strong gravitational field. It is usually admitted that electron–positron pairs fill their magnetosphere. Both plasma and gravity significantly impact on the structure of this magnetosphere. Curvature and frame-dragging effects are indeed important due to the high compactness of neutron stars. For typical models of neutron star interiors, the compactness is about $\Xi = R_s/R \approx 0.5$ where $R_s = 2\,GM/c^2$ is the Schwarzschild radius, M is the mass of the neutron star, R its radius, G the gravitational constant and c the speed of light. From these estimates, we expect a departure from the flat space–time results as large as 15–20 per cent.

Although we are not confronted to the problem of an event horizon as for black hole electrodynamics, frame-dragging effects and curvature of space will distort the magnetic field in the surrounding of the neutron star. As a first step towards a realistic description of neutron star magnetospheres, the force-free approximation is often invoked as a drastic simplification of the problem in the presence of a strongly magnetized plasma. Recently, several groups performed numerical simulations of pulsar magnetospheres in this limit without gravitational effects (Komissarov 2006; McKinney 2006; Spitkovsky 2006; Kalapotharakos, Contopoulos & Kazanas 2012a; Pétri 2012; Parfrey, Beloborodov & Hui 2012).

Our attention now also focuses on the general-relativistic (GR) extension of this force-free picture. Indeed, using a pseudo-spectral discontinuous Galerkin approach, Pétri (2015a) computed GR solutions to the force-free monopole and split monopole fields. Ruiz, Paschalidis & Shapiro (2014) performed the first GR simulations matching the interior solution (within the neutron star) to the exterior solution (the force-free magnetosphere). In a similar way, Pili, Bucciantini & Del Zanna (2015) investigated GR equilibria of neutron stars including twisted magnetic fields by solving a Grad–Shafranov equation. A description of pulsar magnetospheres in terms of Grad–Shafranov equation

was already proposed by Kim et al. (2005) in general relativity in a way similar to black holes in the magnetohydrodynamical (MHD) limit. Abdikamalov, Ahmedov & Miller (2009) and Morozova, Ahmedov & Zanotti (2010) computed the oscillations of the magnetosphere of an aligned rotator in general relativity. Moreover Morozova, Ahmedov & Kagramanova (2008) studied the influence of a monopole on the acceleration of particles in the polar caps extending previous work by Beskin (1990) and Muslimov & Tsygan (1990). Gralla & Jacobson (2014) used tools from differential geometry such as the exterior calculus to deduce some general properties of force-free magnetospheres of black holes and neutron stars. Finally, MHD simulations of neutron star magnetospheres were performed by Komissarov (2006) and later by Tchekhovskoy, Spitkovsky & Li (2013). But these force-free or MHD approaches only represent dissipationless systems not allowing an interchange of energy between the plasma and the electromagnetic field. Therefore, a new degree of freedom is required in the description of the magnetosphere. The resistivity of the plasma could account for such dissipation. It was indeed included in the FFE description by Gruzinov (2008), Kalapotharakos et al. (2012b) , Li, Spitkovsky & Tchekhovskoy (2012) and even in MHD by Palenzuela (2013).

The latest improvements have been made using particle-in-cell (PIC) simulations. As the simplest example, Wada & Shibata (2007, 2011) focused on the plasma electrostatic response to the magnetospheric structure in the aligned dipole rotator using a specially designed electronic chip to efficiently compute the coulomb interactions between charged particles. Special attention to the Y-point was given by Umizaki & Shibata (2010). With this PIC approach, McDonald & Shearer (2009) retrieved the quiet configuration depicted by the electrosphere found by Krause-Polstorff & Michel (1985) and Pétri, Heyvaerts & Bonazzola (2002). On the other hand, full PIC simulations made by Belyaev (2015) show that up to 20 per cent of the spin-down luminosity can be carried by the particle depending on the particle injection rate. Transition from an electrosphere to the force-free magnetosphere is observed depending on the injection process (Philippov & Spitkovsky 2014). Chen & Beloborodov (2014) found the same conclusions by investigation of the aligned magnetosphere including $e^{\pm}$ discharge and radiation. According to Philippov, Spitkovsky & Cerutti (2015), the oblique rotator in PIC simulations also shows a $\sin^2\chi$ dependence as in the force-free limit. Philippov, Tchekhovskoy & Li (2014) also made a comparison between force-free and MHD simulations of the magnetosphere. They were led to the same conclusions. Moreover, they self-consistently computed the torque exerted on the neutron star surface from their simulations. Yuki & Shibata (2012) investigated more deeply polar cap, slot gap, and outer gap models to explain pulsed emission. All the above magnetospheres contain a current sheet wobbling around the equatorial plane, see however Takamori et al. (2014) for an alternative approach to pulsar magnetosphere without this current sheet.

Our goal in this paper is to quantify precisely the distortion induced by GR effects, namely curvature of space–time and frame dragging in the force-free limit. To this end, we solve the time-dependent Maxwell equations in curved space–time in spherical coordinates for a background dipolar magnetic field anchored into the neutron star. Consequently, we use the 3+1 formalism of electrodynamics. The code algorithm is reminded in depth in Section 2. The code is then tested in 1D against known analytical solutions in Cartesian coordinates in Section 3. Application of the code to vacuum and force-free regimes are presented respectively in Sections 4 and 5. Conclusions and ongoing works are drawn in Section 6.

2 NUMERICAL ALGORITHM

Our code is based on a multidomain decomposition technique employing discontinuous Galerkin methods as exposed in Pétri (2015a). This high-order finite volume method was successfully applied to the monopole and split monopole field in the force-free regime. Unknown variables were computed in an orthonormal basis. In our current version of the code, we improved its flexibility by allowing a freedom in the choice of the metric. To this end, we use covariant and contravariant components instead of the physical components to express Maxwell equations, as exposed in the next paragraph. Therefore we are able to compute any kind of electromagnetic structure in a prescribed background curved space in three dimensions once the spatial metric γ_{ab}, the lapse function α and the shift vector $\boldsymbol{\beta}$ have been set up. Remember that in our convention, indexes with letters from a to h span only the absolute space coordinates whereas letters starting from i span the four-dimensional space–time. Details about the implementation of the spatial discretization, the temporal integration, the initial and boundary conditions and the filtering process are given below for completeness.

2.1 Maxwell equations in component form

In order to treat on a same foot any kind of curvilinear coordinate system with the same code, we write Maxwell equations in component form adapted to an absolute space with spatial coordinates x^a and a time coordinate t as described by an observer with four velocity n^i. The time evolution of the electric and magnetic fields, $\boldsymbol{D}$ and $\boldsymbol{B}$, is therefore

$$\partial_t(\sqrt{\gamma}\, D^a) = \varepsilon^{abc}\, \partial_b H_c - \sqrt{\gamma}\, J^a \tag{1a}$$

$$\partial_t(\sqrt{\gamma}\, B^a) = -\varepsilon^{abc}\, \partial_b E_c \tag{1b}$$

with the constitutive relations

$$\varepsilon_0\, E_a = \alpha\, D_a + \varepsilon_0\, c\, \sqrt{\gamma}\, \varepsilon_{abc}\, \beta^b\, B^c \tag{2a}$$

$$\mu_0\, H_a = \alpha\, B_a - \sqrt{\gamma}\, \varepsilon_{abc}\, \beta^b\, D^c/(\varepsilon_0\, c) \tag{2b}$$

and the constraint equations

$$\frac{1}{\sqrt{\gamma}} \, \partial_a(\sqrt{\gamma} \, D^a) = \rho \tag{3a}$$

$$\frac{1}{\sqrt{\gamma}} \, \partial_a(\sqrt{\gamma} \, B^a) = 0. \tag{3b}$$

ε_{abc} and ε^{abc} are the fully antisymmetric three-dimensional Levi–Civita tensors. ε_0 and μ_0 are respectively the vacuum permittivity and permeability. The source terms are the charge density ρ and the current density J^a. The space–time geometry is described by the lapse function α, the shift vector $\boldsymbol{\beta}$ and the spatial metric γ_{ab}, with the definition $\gamma = \det(\gamma_{ab})$. In the slow rotation approximation frequently used for neutron stars, the metric is essentially described by two parameters: the Schwarzschild radius defined by

$$R_s = \frac{2\,G\,M}{c^2} \tag{4}$$

and the spin parameter a_s. A reasonable choice for spherically symmetric and homogeneous neutron stars is

$$\frac{a_s}{R_s} = \frac{2}{5} \frac{R}{R_s} \frac{R}{r_L} \tag{5}$$

where $r_L = c/\Omega$ is the light-cylinder radius and Ω the neutron star rotation rate. The spatial metric is given in spherical Boyer–Lindquist coordinates by

$$\gamma_{ab} = \begin{pmatrix} \alpha^{-2} & 0 & 0 \\ 0 & r^2 & 0 \\ 0 & 0 & r^2 \sin^2 \vartheta \end{pmatrix} \tag{6}$$

the lapse function by

$$\alpha = \sqrt{1 - \frac{R_s}{r}} \tag{7}$$

and the shift vector by

$$c\,\boldsymbol{\beta} = -\omega\,r\,\sin\vartheta\,\boldsymbol{e}_\varphi \tag{8a}$$

$$\omega = \frac{a_s\,R_s\,c}{r^3}. \tag{8b}$$

In contravariant components, the only non-vanishing term of the shift vector is $\beta^\varphi = -\omega/c$. From observations, we have $R \leq 0.1\,r_L$ and realistic equations of state for supranuclear matter gives $R_s \approx 0.5\,R$. In that case the upper limit for the spin parameter would be $a_s \leq 0.08\,R_s \lesssim 0.1\,R_s$. In the remainder of this paper, the spin parameter a_s is constrained by the rotation speed of the neutron star through equation (5). In all the subsequent simulations about neutron star magnetospheres, we will distinguish between two sets of run, the first one concerning electrodynamics in Newtonian gravity with $R_s = a_s = 0$ and the second one including general relativity with a Schwarzschild radius fixed to half the stellar radius R, $R_s = R/2$, and the spin parameter a_s according to equation (5).

We now remind the basic features of our pseudo-spectral discontinuous Galerkin finite element method including the expansion on to vector spherical harmonics for divergencelessness fields, the exact imposition of boundary conditions on the neutron star surface and outgoing waves at the outer boundary, the explicit time stepping with a third order strong stability preserving Runge–Kutta (SSPRK) integration scheme, the spectral filtering in the longitudinal and latitudinal directions and the limiter applied in the radial direction. The radial part is solved with a high-order finite volume scheme whereas the spherical part is solved through a pseudo-spectral approach.

2.2 One-dimensional scalar conservation law

We briefly remind the basic feature of a discontinuous Galerkin approach by focusing on a one dimension non-linear scalar conservation law. Consider therefore a scalar field denoted by u with a physical flux function denoted by $f(u)$ such that the conservation of u is expressed as a partial differential equation written as

$$\partial_t u + \partial_x f(u) = 0. \tag{9}$$

This equation has to be solved for any time $t \geq 0$ and for all $x \in [a, b]$ where $[a, b]$ is the computational domain. Note that in our code x should be interpreted as the radial coordinate r. We subdivide the domain $[a, b]$ in K cells not necessarily of the same length. In each of these cells which we denote by D^k with $k \in [0, \ldots, K - 1]$, the solution is expanded on to a basis of spatial functions ϕ_i^k such that the approximate solution in the cell k reads

$$u^k(x, t) = \sum_{i=0}^{N_p} u_i^k(t)\, \phi_i^k(x) \tag{10}$$

valid in the cell k given by the interval $[x_l^k, x_r^k]$. The basis possesses $N_p + 1$ functions. The spatial method is therefore of order $N_p + 1$. After injecting this expansion into the conservation law equation (9) and projecting on to the basis functions ϕ_i^k, performing two successive integrations by part in each cell independently and introducing a numerical flux f^* we arrive at the semidiscrete system to be solved in matrix notation

$$\mathcal{M}^k \, \partial_t \mathcal{U}^k + \mathcal{S}^k \, \mathcal{F}^k = [(f - f^*) \mathcal{P}^k]_{x_l^k}^{x_r^k} \tag{11}$$

with the following matrices

$$\mathcal{M}_{ij}^k = \int_{x_l^k}^{x_r^k} \phi_i^k \, \phi_j^k \, \mathrm{d}x \tag{12a}$$

$$\mathcal{S}_{ij}^k = \int_{x_l^k}^{x_r^k} \phi_i^k \, \partial_x \phi_j^k \, \mathrm{d}x \tag{12b}$$

that can be computed analytically and exactly and with $\mathcal{P}^k$ the column vector of basis polynomials. Note that for an orthogonal basis, the mass matrix $\mathcal{M}^k$ is diagonal hence very easy to invert. Inverting the mass matrix $\mathcal{M}^k$, each coefficient of the expansion evolves according to the first-order ordinary differential equation

$$\partial_t \mathcal{U}^k + (\mathcal{M}^k)^{-1} \, \mathcal{S}^k \, \mathcal{F}^k = (\mathcal{M}^k)^{-1} \, [(f - f^*) \mathcal{P}^k]_{x_l^k}^{x_r^k}. \tag{13}$$

The state of the art in discontinuous Galerkin methods resides in the choice of the numerical flux f^* which has to satisfy several stability and consistency properties.

2.3 The grid

The arbitrary nature of the radial coordinate is used to fix small volumes close to the neutron star whereas larger shells are sufficient farther away. To be more specific, we employ the usual Fourier transform in the $\{\vartheta, \varphi\}$ directions and expand the radial coordinate into K sub-intervals, the boundary of each cell is given by $[r_g^k, r_d^k]$ with $k \in [0, \ldots, K-1]$ dividing the global interval $[R_1, R_2]$ into non-necessarily equal sub-intervals. Let us assume that the computational domain is comprised between the neutron star surface at $R_1 = R$ and an arbitrary outer radius $R_2 > R_1$. The spherical shell is decomposed into K cells but with increasing thickness. We introduce two temporary variables $y_1 = \log(R_1/r_L)$ and $y_2 = \log(R_2/r_L)$ and a logarithmic thickness by $h = (y_2 - y_1)/K$. Each cell, labelled with a superscript k, possesses then two interfaces located at

$$r_g^k = e^{y_1 + k\,h} \tag{14a}$$

$$r_d^k = e^{y_1 + (k+1)\,h}. \tag{14b}$$

The thickness of the cell labelled k is $h^k = r_d^k - r_g^k$. In that way, the ratio between the size of two successive cells is constant and equal to e^h.

2.4 Vector expansion and divergencelessness constraint on *B*

We use again an expansion of the vector fields *B* and *D*. Indeed, electric and magnetic fields are expanded on to vector spherical harmonics (VSH) according to

$$\boldsymbol{D} = \sum_{l=0}^{\infty} \sum_{m=-l}^{l} \left(D_{lm}^r \, \boldsymbol{Y}_{lm} + D_{lm}^{(1)} \, \boldsymbol{\Psi}_{lm} + D_{lm}^{(2)} \, \boldsymbol{\Phi}_{lm} \right) \tag{15a}$$

$$\boldsymbol{B} = \sum_{l=0}^{\infty} \sum_{m=-l}^{l} \left(B_{lm}^r \, \boldsymbol{Y}_{lm} + B_{lm}^{(1)} \, \boldsymbol{\Psi}_{lm} + B_{lm}^{(2)} \, \boldsymbol{\Phi}_{lm} \right) \tag{15b}$$

Such expansion is done in each cell. However, in order to deal with the divergencelessness of the magnetic field whatever the configuration of the electromagnetic field, loaded or not with plasma it is more appropriate to use an expansion of *B* into

$$\boldsymbol{B} = \sum_{l=1}^{\infty} \sum_{m=-l}^{l} \nabla \times \left[f_{lm}^B(r, t) \, \boldsymbol{\Phi}_{lm} \right] + g_{lm}^B(r, t) \, \boldsymbol{\Phi}_{lm} \tag{16}$$

where $\{f_{lm}^B(r, t), g_{lm}^B(r, t)\}$ are the expansion coefficients of *B*. See Pétri (2013) for more details about vector spherical harmonics.

2.5 Numerical flux

As in any other finite volume scheme, communication between cells goes through a numerical flux f^* chosen to resolve as accurately as possibly the conservation laws. However, for non-linear problems, exact solutions to the associated Riemann problem are usually difficult to

solve and computationally expensive. In order to be as general as possible, we decided to use the simple but robust Lax–Friedrich flux such that

$$f^* = \frac{1}{2} \left[f(u_d^{k-1}) + f(u_g^k) - C(u_g^k - u_d^{k-1}) \right] \tag{17}$$

with the constant $C = \max_u |f'(u)|$ interpreted as the maximum speed for the waves. Fortunately, for high-order methods, the choice of the numerical flux does not impact drastically on the results. Actually, the simulations become insensitive to the exact choice of the flux for high-order methods.

2.6 Slope limiter

The slope limiting technique is adapted from the classical finite volume community. The idea is to reduce spurious oscillations that arise from the non-linear evolution or from sharp discontinuities in the solution. The most basic total variation diminishing (TVD) limiters are usually too dissipative for higher order schemes. Toro (2009) detailed several TVD schemes with application to simple problems. We refer the reader to this book for more information about TVD methods. Another less stringent technique uses a total variation bound (TVB) method (Cockburn, Lin & Shu 1989). The latter does not guaranty strict cancellation of oscillations but only weaken them whereas the former completely avoids oscillations but at the cost of reducing to a low-order scheme. Unfortunately TVB methods introduce one more parameter, often depicted by the capital letter M. Moreover the value of this parameter is very problem dependent, related to the second spatial derivative of the solution, therefore a priori unknown. Eventually we tried another limiting procedure of higher order and called moment limiter, as described by Krivodonova (2007). This technique successively limits the coefficients of the expansions in polynomials from the highest orders down to the lowest coefficients. The limiting is aborted as soon as a coefficient remains unchanged.

2.7 Filtering

The limiter cannot be applied in the latitudinal and longitudinal direction simply because there is no domain decomposition in those directions. We use the classical spherical harmonic expansion. The force-free problem being non-linear due to the electric current in the source terms, we expect the solution to develop sharp gradients or discontinuities also in the spherical directions. It is therefore compulsory to get rid of these high frequencies by some filtering procedure. This is achieved by adding a small damping factor to the high order coefficients of the expansion in Y_{lm}. Filtering is performed at each time step. We use an exponential filter in the directions $\{\vartheta, \varphi\}$ given by the general expression

$$\sigma(\eta) = e^{-\alpha \eta^\beta} \tag{18}$$

where the variable η ranges between 0 and 1. For instance, in the latitudinal direction $\eta = l/(N_\vartheta - 1)$ for $l \in [0, \ldots, N_\vartheta - 1]$, l being the index of the coefficient c_{lm} in the spherical harmonic expansion $f(\vartheta, \varphi) = \sum_{l,m=0}^{N_\vartheta - 1, N_\varphi - 1} c_{lm} Y_{lm}(\vartheta, \varphi)$ and $\{N_\vartheta, N_\varphi\}$ the number of collocation points in the spherical direction (latitude and longitude). The parameter α (not to be confused with the lapse function) is adjusted to values not too large in order to avoid errors in the solution but also not too small in order to sufficiently damp oscillations.

The above mentioned exponential filter of order β does not strictly satisfy the condition for the smoothing factors as explained in Canuto et al. (2006). However, for numerical purposes we choose α such that $e^{-\alpha}$ is numerically zero i.e. below the machine accuracy ε. In practice, we choose $\alpha = 36$ assuming double precision computation with $\epsilon \approx 10^{-15}$. The order β of the smoothing influences the dissipation rate in the solution. The low-order multipole components are weakly damped and correspond to large scale structures. If the solution shows fine scale structures, the filtering has to be minimized.

2.8 Time integration

One of the strength of pseudo-spectral methods is that they replace a set of partial differential equations (PDE) by a larger set of ordinary differential equations (ODE) for the unknown collocation points or spectral coefficients. Schematically, it can be written as

$$\frac{d\boldsymbol{u}}{dt} = f(t, \boldsymbol{u}) \tag{19}$$

with appropriate initial and boundary conditions. $\boldsymbol{u}$ represents the vector of unknown functions either evaluated at the collocation points or the spectral coefficients. We use a third order SSPRK scheme advancing the unknown functions $\boldsymbol{u}$ in time. See Hesthaven & Warburton (2008) for more details about these time integration schemes especially including the popular second- and third-order symbolically written as SSPRK2 and SSPRK3.

2.9 Boundary conditions

As in Pétri (2014), we put exact boundary conditions on the star. In general relativity, the correct jump conditions at the stellar surface, continuity of the normal component of the magnetic field B^r and continuity of the tangential component of the electric field $\{D^\vartheta, D^\varphi\}$ are such that

$$B^r(t, R, \vartheta, \varphi) = B_0^r(t, \vartheta, \varphi) \tag{20a}$$

$$D^{\vartheta}(t, R, \vartheta, \varphi) = -\varepsilon_0 \frac{\Omega - \omega}{\alpha^2} \sin\vartheta \, B_0^r(t, \vartheta, \varphi) \tag{20b}$$

$$D^{\varphi}(t, R, \vartheta, \varphi) = 0. \tag{20c}$$

Note the slight difference in these expressions with respect to our previous papers because here we use tensor components in a non-orthonormal basis. The continuity of B^r automatically implies the correct boundary treatment of the electric field. $B_0^r(t, \vartheta, \varphi)$ represents the, possibly time dependent, radial magnetic field imposed by the star, let it be monopole, split monopole, oblique dipole or multipole.

Maxwell equations, explicitly written, are

$$\partial_t(\sqrt{\gamma}\, D^r) = \partial_\vartheta H_\varphi - \partial_\varphi H_\vartheta - \sqrt{\gamma}\, J^r \tag{21a}$$

$$\partial_t(\sqrt{\gamma}\, D^\vartheta) = \partial_\varphi H_r - \partial_r H_\varphi - \sqrt{\gamma}\, J^\vartheta \tag{21b}$$

$$\partial_t(\sqrt{\gamma}\, D^\varphi) = \partial_r H_\vartheta - \partial_\vartheta H_r - \sqrt{\gamma}\, J^\varphi \tag{21c}$$

$$\partial_t(\sqrt{\gamma}\, B^r) = \partial_\varphi E_\vartheta - \partial_\vartheta E_\varphi \tag{21d}$$

$$\partial_t(\sqrt{\gamma}\, B^\vartheta) = \partial_r E_\varphi - \partial_\varphi E_r \tag{21e}$$

$$\partial_t(\sqrt{\gamma}\, B^\varphi) = \partial_\vartheta E_r - \partial_r E_\vartheta. \tag{21f}$$

We look for the characteristics propagating along the radial direction. To this end, we isolate expressions containing the radial propagation that is ∂_r and ∂_t. Eliminating all useless terms for this radial propagation, the system reduces to

$$\partial_t(\sqrt{\gamma}\, D^\vartheta) + \partial_r H_\varphi = 0 \tag{22a}$$

$$\partial_t(\sqrt{\gamma}\, D^\varphi) - \partial_r H_\vartheta = 0 \tag{22b}$$

$$\partial_t(\sqrt{\gamma}\, B^\vartheta) - \partial_r E_\varphi = 0 \tag{22c}$$

$$\partial_t(\sqrt{\gamma}\, B^\varphi) + \partial_r E_\vartheta = 0. \tag{22d}$$

The covariant components of the spatial vectors $\boldsymbol{D}$ and $\boldsymbol{B}$ are giving by lowering the indexes such that

$$D_\vartheta = \gamma_{\vartheta r}\, D^r + \gamma_{\vartheta\vartheta}\, D^\vartheta + \gamma_{\vartheta\varphi}\, D^\varphi \tag{23a}$$

$$D_\varphi = \gamma_{\varphi r}\, D^r + \gamma_{\varphi\vartheta}\, D^\vartheta + \gamma_{\varphi\varphi}\, D^\varphi \tag{23b}$$

$$B_\vartheta = \gamma_{\vartheta r}\, B^r + \gamma_{\vartheta\vartheta}\, B^\vartheta + \gamma_{\vartheta\varphi}\, B^\varphi \tag{23c}$$

$$B_\varphi = \gamma_{\varphi r}\, B^r + \gamma_{\varphi\vartheta}\, B^\vartheta + \gamma_{\varphi\varphi}\, B^\varphi. \tag{23d}$$

Injecting the constitutive relations into the evolution equations, we find

$$\partial_t(\sqrt{\gamma}\, \mu_0\, D^\vartheta) + \partial_r(\alpha\, B_\varphi) - \partial_r\left(\frac{\sqrt{\gamma}}{\varepsilon_0\, c}\, (\beta^r\, D^\vartheta - \beta^\vartheta\, D^r)\right) = 0 \tag{24a}$$

$$\partial_t(\sqrt{\gamma}\, \mu_0\, D^\varphi) - \partial_r(\alpha\, B_\vartheta) + \partial_r\left(\frac{\sqrt{\gamma}}{\varepsilon_0\, c}\, (\beta^\varphi\, D^r - \beta^r\, D^\varphi)\right) = 0 \tag{24b}$$

$$\partial_t(\sqrt{\gamma}\, \varepsilon_0\, B^\vartheta) - \partial_r(\alpha\, D_\varphi) - \partial_r(\varepsilon_0\, c\, \sqrt{\gamma}\, (\beta^r\, B^\vartheta - \beta^\vartheta\, B^r)) = 0 \tag{24c}$$

$$\partial_t(\sqrt{\gamma}\, \varepsilon_0\, B^\varphi) + \partial_r(\alpha\, D_\vartheta) + \partial_r(\varepsilon_0\, c\, \sqrt{\gamma}\, (\beta^\varphi\, B^r - \beta^r\, B^\varphi)) = 0. \tag{24d}$$

Defining the unknown vector

$$U = \begin{pmatrix} \sqrt{\gamma}\,\mu_0\,D^\vartheta \\ \sqrt{\gamma}\,\mu_0\,D^\varphi \\ \sqrt{\gamma}\,\varepsilon_0\,B^\vartheta \\ \sqrt{\gamma}\,\varepsilon_0\,B^\varphi \end{pmatrix} \tag{25}$$

the system can be cast into the conservative form $\partial_t U + \partial_r(A\,U) = 0$ with

$$A = \begin{pmatrix} -c\,\beta^r & 0 & \alpha\,\gamma_{\varphi\vartheta}/(\varepsilon_0\,\sqrt{\gamma}) & \alpha\,\gamma_{\varphi\varphi}/(\varepsilon_0\,\sqrt{\gamma}) \\ 0 & -c\,\beta^r & -\alpha\,\gamma_{\vartheta\vartheta}/(\varepsilon_0\,\sqrt{\gamma}) & -\alpha\,\gamma_{\varphi\vartheta}/(\varepsilon_0\,\sqrt{\gamma}) \\ -\alpha\,\gamma_{\varphi\vartheta}/(\mu_0\,\sqrt{\gamma}) & -\alpha\,\gamma_{\varphi\varphi}/(\mu_0\,\sqrt{\gamma}) & -c\,\beta^r & 0 \\ \alpha\,\gamma_{\vartheta\vartheta}/(\mu_0\,\sqrt{\gamma}) & \alpha\,\gamma_{\vartheta\varphi}/(\mu_0\,\sqrt{\gamma}) & 0 & -c\,\beta^r \end{pmatrix}. \tag{26}$$

We restrict ourselves to metrics with vanishing components $\gamma_{\vartheta\varphi}$. Therefore, the eigenvalues for the electromagnetic waves propagating in vacuum in general relativity are given by

$$\left(-\beta^r \pm \alpha\,\sqrt{\frac{\gamma_{\vartheta\vartheta}\,\gamma_{\varphi\varphi}}{\gamma}} \right) c \tag{27}$$

and the eigenvectors by

$$\left(\pm\sqrt{\frac{\gamma_{\varphi\varphi}\,\mu_0}{\gamma_{\vartheta\vartheta}\,\varepsilon_0}}, 0, 0, 1 \right) \quad \left(0, \pm\sqrt{\frac{\gamma_{\vartheta\vartheta}\,\mu_0}{\gamma_{\varphi\varphi}\,\varepsilon_0}}, 1, 0 \right). \tag{28}$$

For the slowly rotating metric in spherical Boyer–Lindquist coordinates these expressions simplify for the wave speed

$$(-\beta^r \pm \alpha^2)\,c \tag{29}$$

and for the conserved quantities propagating along the characteristics

$$\varepsilon_0\,c\,\sin\vartheta\,B^\varphi \pm D^\vartheta \tag{30a}$$

$$\varepsilon_0\,c\,B^\vartheta \pm \sin\vartheta\,D^\varphi\,. \tag{30b}$$

The outer boundary condition cannot be handled exactly. We need to make some approximate assumptions about the outgoing waves we want to enforce in order to prevent reflections from this artificial outer boundary. Using the Characteristic Compatibility Method (CCM) described in Canuto et al. (2007) and neglecting the frame-dragging effect far from the neutron star, the radially propagating characteristics are given to good accuracy by their flat space–time expressions as

$$D^\vartheta \pm \varepsilon_0\,c\,\sin\vartheta\,B^\varphi; \qquad \sin\vartheta\,D^\varphi \pm \varepsilon_0\,c\,B^\vartheta. \tag{31}$$

In order to forbid ingoing waves, we ensure that

$$D^\vartheta - \varepsilon_0\,c\,\sin\vartheta\,B^\varphi = 0 \tag{32a}$$

$$\sin\vartheta\,D^\varphi + \varepsilon_0\,c\,B^\vartheta = 0 \tag{32b}$$

whereas the other two characteristics are found by

$$D^\vartheta + \varepsilon_0\,c\,\sin\vartheta\,B^\varphi = D^\vartheta_{\text{PDE}} + \varepsilon_0\,c\,\sin\vartheta\,B^\varphi_{\text{PDE}} \tag{32c}$$

$$\sin\vartheta\,D^\varphi - \varepsilon_0\,c\,B^\vartheta = \sin\vartheta\,D^\varphi_{\text{PDE}} - \varepsilon_0\,c\,B^\vartheta_{\text{PDE}} \tag{32d}$$

the subscript PDE denoting the values of the electromagnetic field obtained by straightforward time advancing without care of any boundary condition. The new corrected values are deduced from the solution of the linear system made of equations (32a)–(32d).

2.10 Initial conditions

The rotation of the neutron star is switched on smoothly as in our previous works, see Pétri (2012, 2014, 2015a). Its spin frequency increases slowly starting from zero. Taking an evolution of the spin frequency as

$$\Omega(t) = \begin{cases} \sin^2\left(\frac{t}{8}\right) & \text{for } t \le 4\pi \\ 1 & \text{for } t \ge 4\pi \end{cases} \tag{33}$$

starting at zero speed avoids the initial discontinuity in the electric field. The normalized period at full rotation speed is 2π. The spin frequency as well as its first derivative are smooth at the initial time of the simulation $t = 0$. The final time of all simulation runs is set to $T_f = 12\pi$ and corresponds to five full rotations of the neutrons star. This is sufficient for the system to settle down to its quasi-stationary state.

3 TESTS

In our update of the discontinuous Galerkin code, we use a tensorial (covariant) formalism to compute the vector components in order to specify freely the background metric. It is therefore possible to describe any kind of coordinate system through this metric. In particular, we can test our code in a one dimensional Cartesian coordinate system and compare our simulation results with exact analytical solutions in the force-free limit. To this aim, several special cases are usually checked as reported in Komissarov (2002, 2004) and in Paschalidis & Shapiro (2013).

We performed our tests starting with the initial conditions given in these aforementioned works. For completeness, we reproduce these test cases in the subsequent paragraphs. Results are shown in Figs 1 and 2. The simulation points are indicated with blue crosses whereas the analytical solutions, if they exist, are shown in red solid line. For simulation purposes, we use normalized units for the electromagnetic field by setting $c = \mu_0 = \varepsilon_0 = 1$. The background metric is Minkowski space–time in Cartesian coordinates. Let us describe shortly each case. From the analysis of force-free electrodynamics, as reported by Komissarov (2002), we expect only two kind of waves: fast waves that are similar to electromagnetic waves in vacuum and Alfvén waves similar to those of relativistic MHD. We do not follow strictly the initial conditions prescribed in the above literature, instead of a linear or sinusoidal variation when required, we preferred a tangent hyperbolic spatial dependence.

3.1 Alfven wave

Alfvén waves are important solutions to force-free electrodynamics. In the frame of the wave itself, the initial conditions are given by

$$\phi = 1.15 + 0.15 \tanh(10\,x) \tag{34a}$$

$$E'_x = -c\,B'_z = -\phi \tag{34b}$$

$$E'_y = 0 \tag{34c}$$

$$E'_z = B'_x = B'_y = 1. \tag{34d}$$

These expressions need to be boosted into the observer frame via a Lorentz transform. The wave therefore propagates to the left at a speed given in the observer frame by 0.5. The simulation results are shown in Fig. 1, upper panel. The wave speed is accurately caught by our algorithm.

3.2 Current sheet

A current sheet corresponds to a solution with an initial discontinuity in the magnetic field. As a starting point, we use the following setup

$$B_y = \begin{cases} B_0 & \text{if } x \leq 1 \\ -B_0 & \text{if } x \geq 1 \end{cases} \tag{35a}$$

$$E_x = E_y = E_z = B_z = 0 \tag{35b}$$

$$B_x = 1. \tag{35c}$$

The temporal evolution will then depend on the value of B_0. In the first run, we used $B_0 = 0.5$. This launches two fast waves moving in opposite directions at the speed of light, see second panel from top of Fig. 1. In a second run we used $B_0 = 2$. Two fast waves are still allowed but force-free electrodynamics has no solution, see middle panel of Fig. 1.

3.3 Degenerate Alfvén wave

A degenerate Alfvén wave can be produced in the following manner. In the frame of the wave itself, the initial conditions are given by

$$\phi = \pi\,\frac{1 + \tanh(10\,x)}{4} \tag{36a}$$

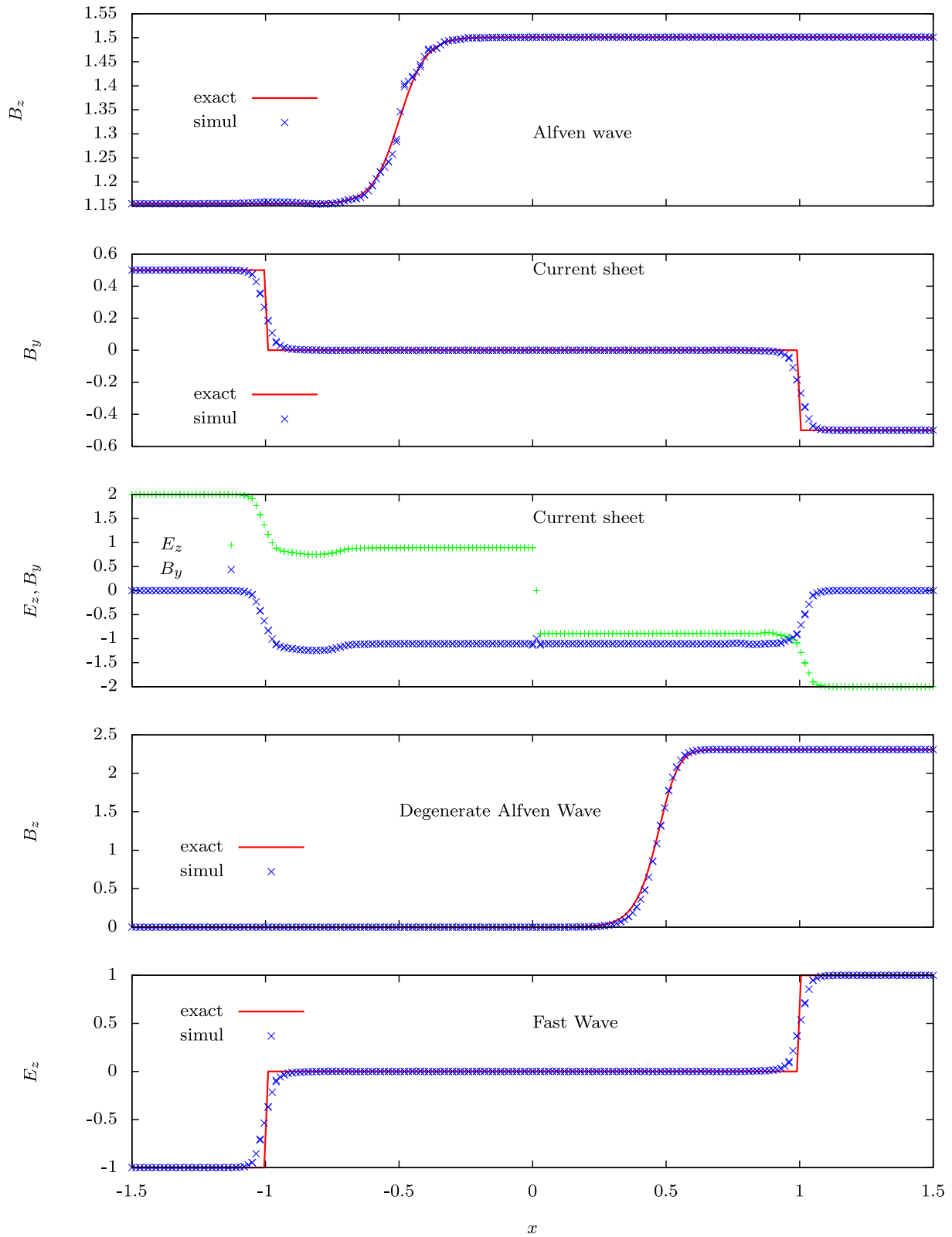$$E'_x = E'_y = E'_z = 0 = c\,B'_x \tag{36b}$$

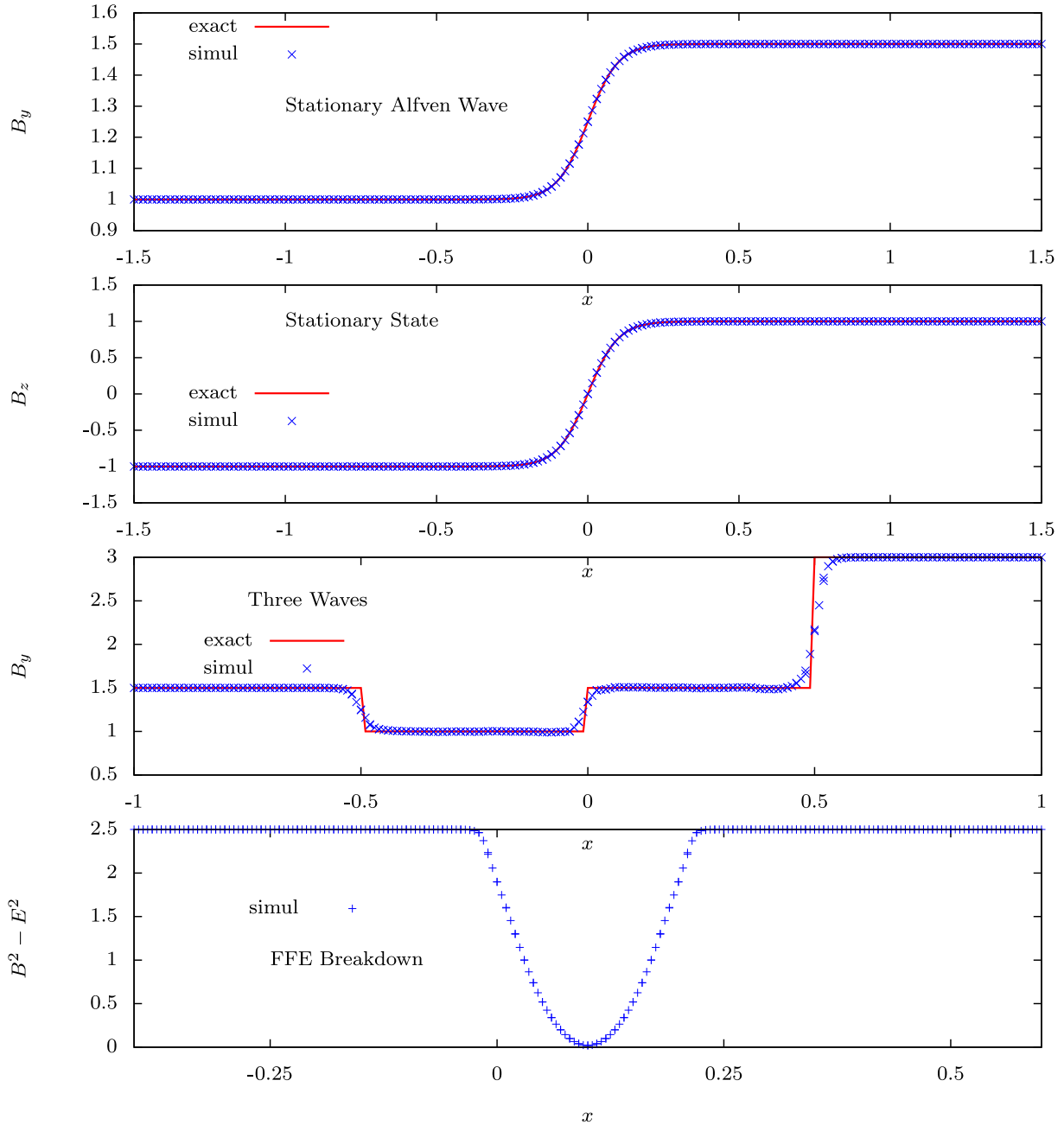**Figure 1.** Numerical test of the code for several 1D Cartesian problems, first set.

Figure 2. Numerical test of the code for several 1D Cartesian problems, second set.

$$B'_y = 2 \cos \phi \tag{36c}$$

$$B'_z = 2 \sin \phi. \tag{36d}$$

These expressions need to be boosted into the observer frame via a Lorentz transform. The wave therefore propagates to the right at a speed given in the observer frame by 0.5, see second panel from the bottom of Fig. 1.

3.4 Fast wave

This test corresponds to two fast waves given initially by a discontinuity at $x = 0$ such that

$$E_z = -c\, B_y = \begin{cases} 1 & \text{if } x \leq 1 \\ -1 & \text{if } x \geq 1 \end{cases} \tag{37a}$$

$$E_x = E_y = B_z = 0 \tag{37b}$$

$$B_x = 1. \tag{37c}$$

One propagates to the right and the other to the left, both at the speed of light. We have chosen a discontinuity to show the effect of filtering on a discontinuous solution. The smoothing is clearly apparent in the lower panel of Fig. 1 but the speed of the wave is exactly reproduced.

3.5 Stationary Alfvén wave

An Alfvén wave with zero speed is given by

$$\phi = 1.25 + 0.25 \tanh(10 \, x) \tag{38a}$$

$$E_x = -c \, B_y = -\phi \tag{38b}$$

$$E_y = c \, B_x = 1 \tag{38c}$$

$$E_z = 0.0 \tag{38d}$$

$$B_z = 2. \tag{38e}$$

It corresponds to a stationary Alfvén state remaining in our example around $x = 0$ as seen in the upper panel of Fig. 2.

3.6 Stationary state

This test corresponds to a stationary state given by

$$E_x = c \, B_z = \tanh(10 \, x) \tag{39a}$$

$$E_y = E_z = B_x = 0 \tag{39b}$$

$$B_y = 1. \tag{39c}$$

No time evolution is expected. The only effect could be a smearing due to numerical dissipation caused by our filtering procedure. Actually, inspecting the second panel from top of Fig. 2, the stationary state is maintained to very good accuracy for a long time.

3.7 Three waves

It is possible to get two fast waves propagating in opposite direction and a stationary Alfvén wave in the same run for the special initial conditions given by

$$\boldsymbol{B} = \begin{cases} (1, 1.5, 3.5) & \text{if } x \leq 0 \\ (1, 3, 3) & \text{if } x > 0 \end{cases} \tag{40a}$$

$$\boldsymbol{E} = \begin{cases} (-1, -0.5, 0.5) & \text{if } x \leq 0 \\ (-1.5, 2, -1.5) & \text{if } x > 0 \end{cases} \tag{40b}$$

This magnetic configuration splits into two fast discontinuities propagating in opposite directions at the speed of light and a stationary Alfvén wave staying at $x = 0$, second panel from bottom of Fig. 2.

3.8 FFE breakdown

In some cases, the FFE approximation can be violated during the evolution process of the plasma. For instance, with the initial conditions given by

$$\boldsymbol{B} = \begin{cases} (1, 1, 1) & \text{if } x \leq 0 \\ (1, 1 - 10 \, x, 1 - 10 \, x) & \text{if } 0 \geq x \leq 0.2 \\ (1, -1, -1) & \text{if } x \geq 0.2 \end{cases} \tag{41a}$$
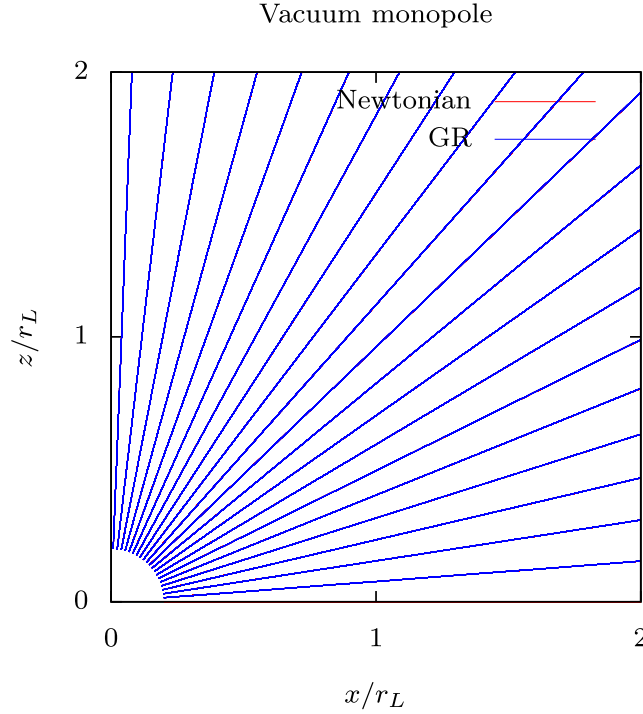
Vacuum monopole

Figure 3. Meridional field lines for the vacuum monopole in flat space–time, red line and in the slow rotation approximation, blue line, with $R/r_L = 0.2$. The Newtonian case and the relativistic case overlap perfectly.

$$\boldsymbol{E} = (0, 0.5, -0.5). \tag{41b}$$

after a short time of about $\Delta t = 0.02$, the requirement $E^2 < B^2$ everywhere becomes difficult to be fulfilled. $B^2 - E^2$ starts to vanish around $x = 0.1$, bottom panel of Fig. 2.

Going through all the above tests, we showed that the code reproduces the expected analytical solutions to good accuracy. We switch now to the 3D spherical case concerning neutron star electromagnetic fields.

4 VACUUM MAGNETOSPHERES

Before going to the most interesting case of a force-free pulsar magnetosphere, we check again our algorithm against known vacuum solutions, given exactly in flat space–time and to high accuracy in curved space–time. In all the simulations shown below, the Poynting flux $\boldsymbol{S}$ is used as an efficient and simple diagnostic tool to check the convergence of the code. For comparison between different magnetic topologies as well as for the discrepancies between Newtonian (N) and GR cases, this luminosity is always computed through a sphere $\mathcal{S}_L$ of radius equal to the light-cylinder radius thus

$$L = \int_{\mathcal{S}_L} (\boldsymbol{E} \wedge \boldsymbol{H})^{\hat{r}} \, \mathrm{d}S \tag{42}$$

where the hat $\hat{r}$ means the physical component of the Poynting vector and $\mathrm{d}S = r^2 \, \mathrm{d}\Omega$ the infinitesimal surface element on the sphere $\mathcal{S}_L$ and $\mathrm{d}\Omega$ the solid angle.

4.1 Monopole

The monopole field represents the archetypal solution for which an exact analytical expression exists in flat space–time, in vacuum but most importantly for the force-free rotator. It serves as a good test of efficiency and accuracy of any algorithm. Thus we started with a monopole field in vacuum. The results found by our numerical code agree well with the analytical expressions. As an illustration, we show some magnetic field lines in the meridional plane for the Newtonian case $R_s = 0$ and the slow rotation approximation with $R_s/R = 0.5$ in Fig. 3 for a rotator possessing a rotational speed in normalized units given by $R/r_L = 0.2$. The radial structure of the field topology is not influenced by general relativity. The field lines remain straight as in flat space–time. Indeed, the radial component of the magnetic field is the only non-vanishing part and is simply expressed by

$$B^r = \alpha \, B \, \frac{R^2}{r^2} \tag{43}$$
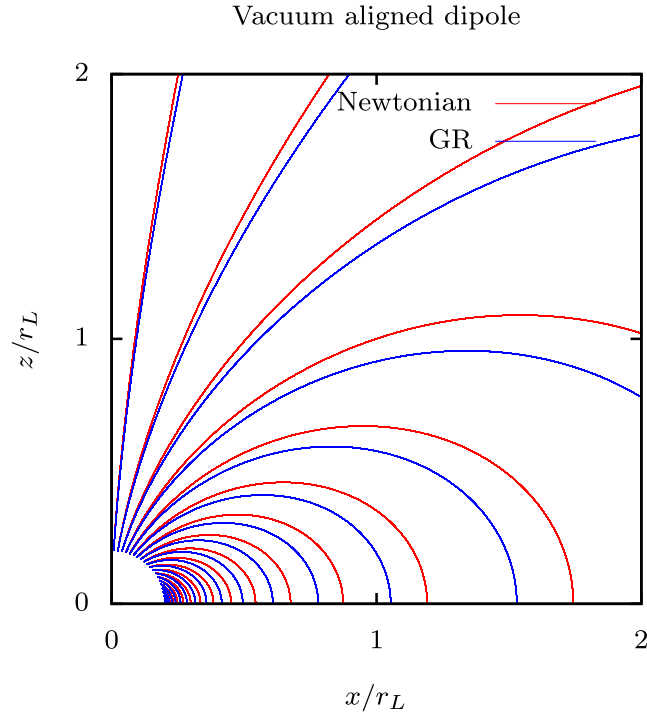
Vacuum aligned dipole

Figure 4. Meridional field lines for the vacuum aligned dipole in flat space–time, red line and in the slow rotation approximation, blue line, with $R/r_L = 0.2$. The location of the foot of each line is the same in both runs.

where B is the magnetic field strength as measured by a distant observer. The Poynting flux vanishes after a transition phase during which the electric field builds up to its final stage.

4.2 Dipole

The lowest order magnetic field topology anchored into a neutron star is dipolar. Thus, we investigate the case of an aligned dipole in vacuum. Magnetic field lines in the meridional plane for the Newtonian case and the slow rotation approximation are depicted in Fig. 4 for $R/r_L = 0.2$. Compared to flat space–time, general relativity compresses the field lines towards the equatorial plane. The Poynting flux here also vanishes due to the axisymmetry of the configuration.

The oblique rotator is the most interesting case for neutron star magnetosphere. It represents the lowest order multipole anchored in the star although higher order multipoles could exist, see Pétri (2015b). As a special case, we investigate the perpendicular rotator. In order to get an idea of the magnetic field topology, field lines contained in the equatorial plane are shown in Fig. 5, comparing again the Newtonian dipole and the slow rotation dipole with $R/r_L = 0.2$. The typical spin-down luminosity, used for normalization, is given by the orthogonal vacuum rotator

$$L_{\rm dip}^{\rm vac} = \frac{8\pi}{3} \frac{\Omega^4 \, B^2 \, R^6}{\mu_0 \, c^3}. \tag{44}$$

To conclude the vacuum simulations, we performed a set of simulations for oblique rotators in the case $R/r_L = \{0.1, 0.2, 0.5\}$ and for $\chi = \{0°, 15°, 30°, 45°, 60°, 75°, 90°\}$ to check the dependence of the luminosity on the geometry. The results are reported in Fig. 6 for the Newtonian, red symbols, and GR, blue symbols, gravitational fields. The points are taken from the simulations whereas the solid curves are best fits obtained by adjusting to a $\sin^2 \chi$ dependence such that

$$\frac{L}{L_{\rm dip}^{\rm vac}} = b \, \sin^2 \chi. \tag{45}$$

The precise values are reported in Table 1 comparing Newtonian and GR gravity. As the ratio R/r_L decreases, both kind of curves, Newtonian and GR, tend to the function $\sin^2 \chi$, the former from below and the latter from above.

As a final comparison, we plot the Poynting fluxes expected from the Deutsch solution and the simulations in Fig. 7. We are able to go down to rotation rates as low as $R/r_L = 0.01$ allowing us to span an appreciable range of rotation periods. The Poynting flux of the vacuum orthogonal rotator is reported in Fig. 7 for periods between $R/r_L = 0.01$ and 0.5. Adjusting the absolute Poynting in Fig. 8 with a power we can estimate the braking index. Indeed, the associated estimated braking indexes for the Deutsch solution and the simulation are respectively $n = 3.05$ and $n = 2.93$. Consequently, the point dipole braking index in vacuum, known to be equal to $n = 3$ is retrieved to good accuracy in the GR case. The increase in total luminosity can in part be explained by the increase in the transverse magnetic field in the vicinity of the
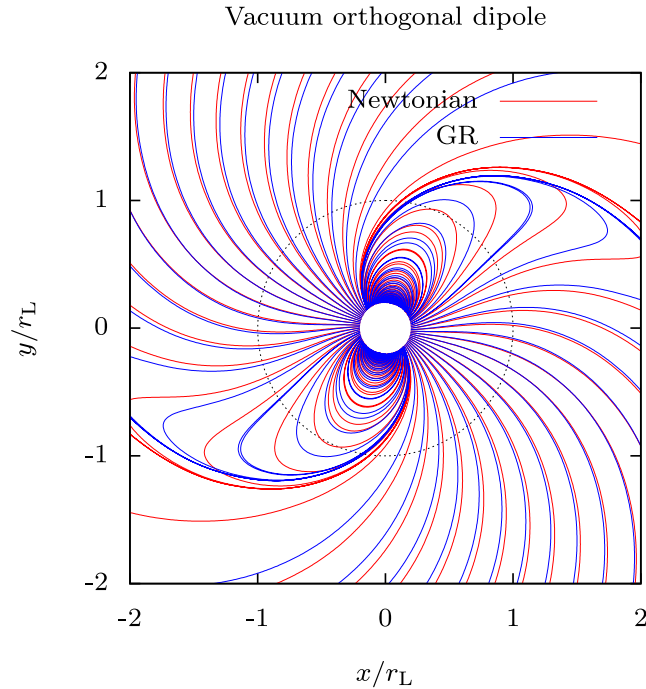
Vacuum orthogonal dipole

Figure 5. Equatorial field lines for the vacuum perpendicular dipole in flat space–time, red line, and in the slow rotation approximation, blue line, with $R/r_L = 0.2$.
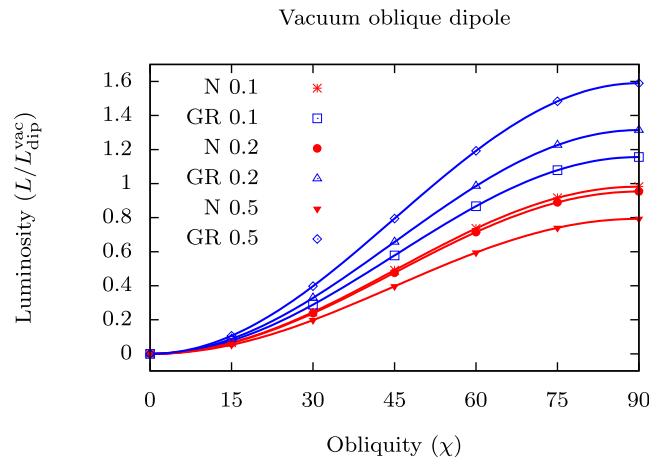
Vacuum oblique dipole

Figure 6. Poynting flux of the vacuum oblique rotator for different obliquities χ and normalized to L_{dip}^{vac} with $R/r_L = \{0.1, 0.2, 0.5\}$. Points are taken from the simulations and the solid lines are the best fits, Newtonian in red (N) and general-relativistic in blue (GR).

Table 1. Best-fitting parameter b for the Poynting flux $L(\chi)/L_{dip}^{vac} = b \sin^2 \chi$ of the vacuum dipole rotator in Newtonian and GR case.

R/r_L	Newtonian	GR
0.1	0.982	1.156
0.2	0.955	1.316
0.5	0.793	1.590

light cylinder. Indeed, in Fig. 9 we compute the ratio L_{GR}/L_{Newt} as a solid red curve. We observe an increase by a factor two for the fastest rotator with $R/r_L = 0.5$. Meanwhile, we compared this increase of luminosity to the increase in the physical components of the transverse magnetic field components $\{B^{\hat{\vartheta}}, B^{\hat{\varphi}}\}$ at the light cylinder as predicted by the GR vacuum dipole solution, see the green curve in Fig. 9 and also Rezzolla & Ahmedov 2004. Within 10–15 per cent the increase in luminosity is explained by the strength of the magnetic field at the

Vacuum orthogonal dipole
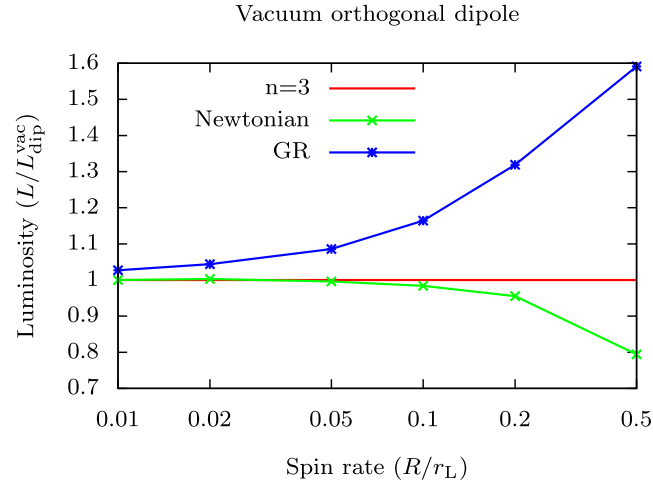
Figure 7. Poynting flux of the vacuum orthogonal rotator normalized to L_{dip}^{vac}. The different approximations are shown in green for Newtonian and blue for GR and compared to a braking index of $n = 3$ in red.

Vacuum orthogonal dipole
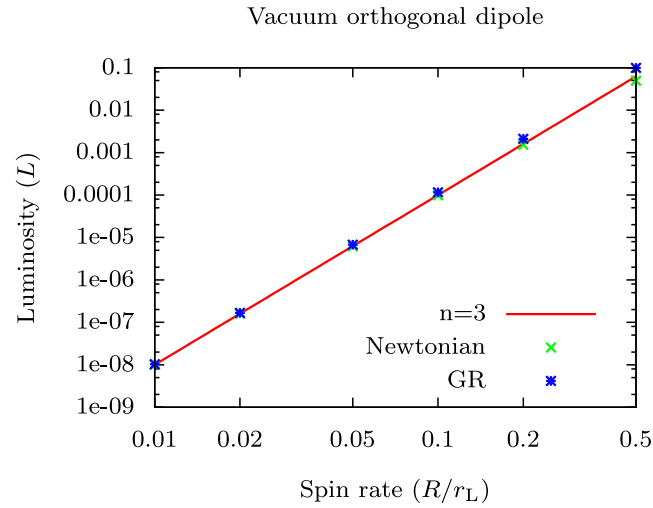
Figure 8. Absolute Poynting flux of the vacuum orthogonal dipole rotator. The different approximations are marked by symbols, green for Newtonian and blue for GR and compared to the point dipole expectations for which $n = 3$ in red.

Vacuum orthogonal dipole
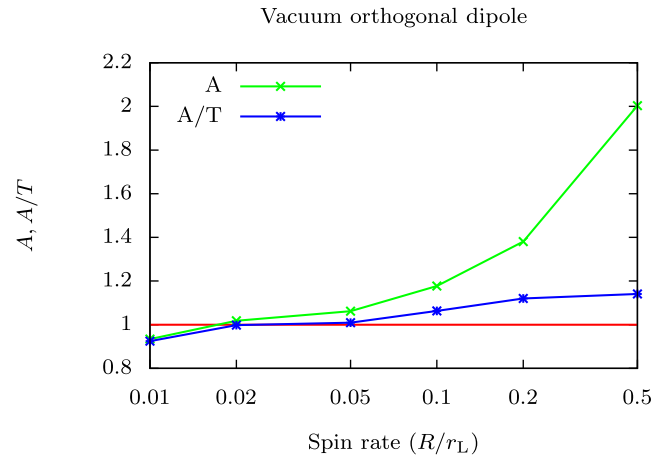
Figure 9. Comparison of the increase in total luminosity as obtained by the simulation through the amplification factor $A = L_{GR}/L_{Newt}$, green solid curve, and as predicted by the increase in the transverse magnetic field $A/T = (L_{GR}/L_{Newt})/$theory, blue solid curve. For reference, the line $L = 1$ is also shown in red.

Vacuum orthogonal dipole
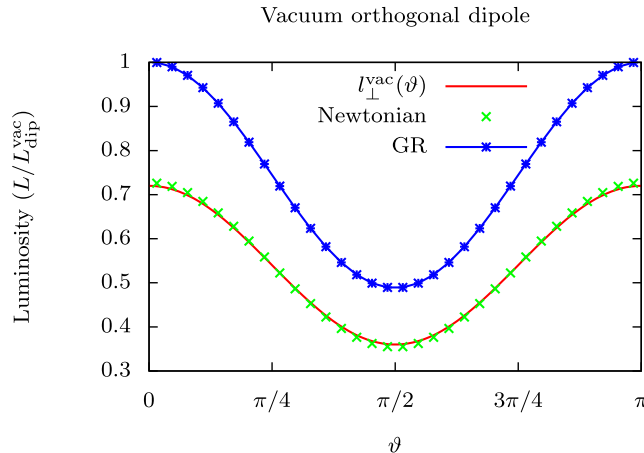
Figure 10. Angular dependence of the Poynting flux for the vacuum perpendicular dipole in flat space–time and in the slow rotation approximation with $R/r_L = 0.2$. It corresponds to the flux through the sphere of radius $5\,r_L$.

light cylinder. Note that we do not take into account possible frame-dragging effects that are stronger for the fastest rotators, explaining the discrepancies for the highest R/r_L.

The angular dependence of the Poynting flux normalized to the total luminosity for a point dipole is given for any inclination $\chi > 0$ at large distance $r \gg r_L$ by

$$l_\perp^{vac}(\vartheta) = \frac{L(\vartheta)}{L_{dip}^{vac}} = \frac{3}{8}\,(1 + \cos^2\vartheta)\left[1 - \left(\frac{R}{r_L}\right)^2\right] \tag{46}$$

Note that it is independent of the inclination angle χ and takes into account corrections in power of R/r_L. For the vacuum perpendicular dipole, in Fig. 10, this analytical expression is shown in solid red line and compared to the Newtonian simulations, green crosses, and to its GR extension, blue stars. This Poynting flux is extracted from the sphere of radius $r = 5\,r_L$. All the angular dependences of the luminosity shown in this paper are given at this particular radius.

5 FORCE-FREE MAGNETOSPHERES

The most interesting results concern the plasma screening effect in the pulsar magnetosphere. This is investigated in the force-free approximation as a starting point. Full general relativity is account for by the 3+1 formalism already employed in previous works. We revisit the GR monopole and split monopole cases before diving into the dipole rotator for arbitrary inclination.

5.1 Monopole

The monopole field is simply described by a radial component decreasing like an inverse square law. This expression is valid in flat as well as in curved space–time. In Boyer–Lindquist coordinates, there is no distinction between both topologies. Indeed, inspecting Fig. 11, the field lines in the meridional plane overlap whatever the rotation rate R/r_L. Nevertheless, the Poynting flux, as measured by a distant observer, decreases slightly with increasing spin rate as seen in Fig. 12. To finish the discussion with this set of simulations, the braking indexes for the Newtonian and GR monopole solutions are compared and equal respectively to $n = 3.000$ and $n = 2.996$, obtained from fitting the absolute Poynting flux shown in Fig. 13 to a power law in R/r_L. The angular dependence of the Poynting flux for the force-free monopole normalized to its total luminosity, which is equivalent to the perpendicular vacuum dipole rotator luminosity, is equal to

$$l_{mono}^{vac}(\vartheta) = \frac{L(\vartheta)}{L_{dip}^{vac}} = \frac{3}{4}\,\sin^2\vartheta \tag{47}$$

and represented in Fig. 14. The analytical expression in solid red line overlaps with the Newtonian simulations depicted by green crosses and also with the GR simulations in blue stars. In order to investigate the influence of the numerical resolution on the accuracy of the simulations, we plot the Poynting flux for the force-free monopole in Fig. 15 for different resolutions by increasing the number of colatitudinal points N_ϑ in the GR case and for $R/r_L = 0.2$. Because the solution does not contain any discontinuity, already a low resolution gives satisfactory results. The error is less than 1 per cent.

5.2 Split monopole

The meridional magnetic field lines for the split monopole field are shown in Fig. 16. Here again, as in the monopole case, the configuration in Boyer–Lindquist coordinates are not distinguishable. The associated Poynting flux should be the same as for the monopole case. This
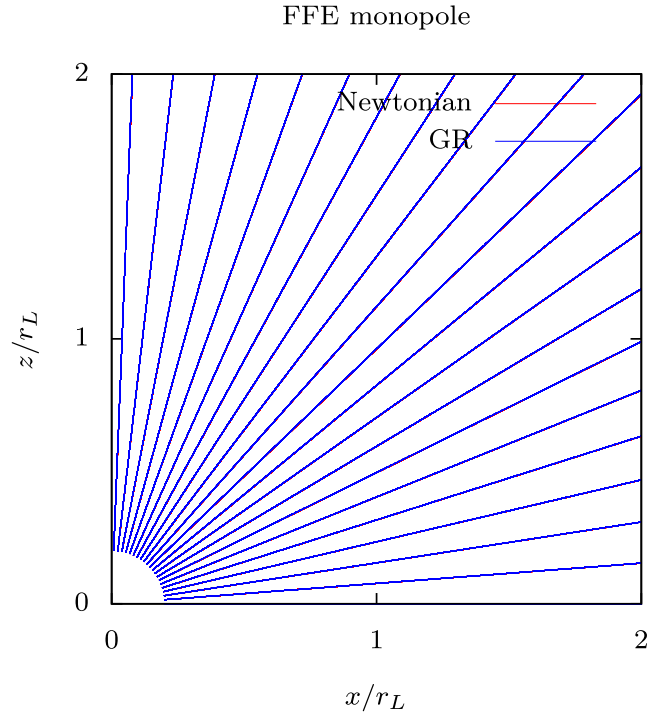
FFE monopole

Figure 11. Meridional field lines for the force-free monopole in flat space–time, red curve, and in the slow rotation approximation, blue curve. The period of the neutron star is such that $R/r_L = 0.2$. Field lines overlap exactly.
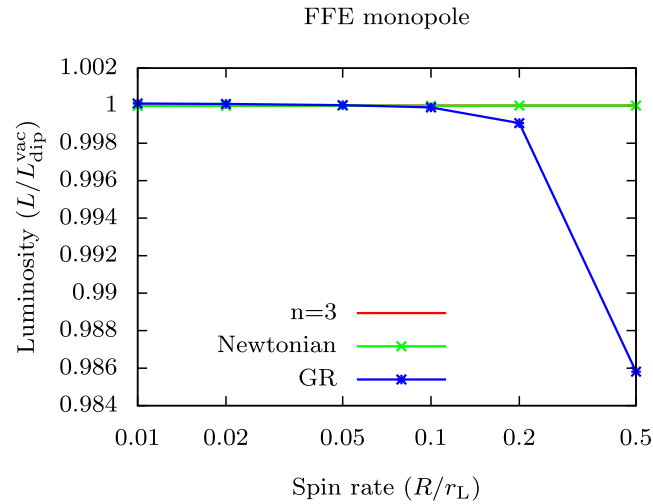
FFE monopole

Figure 12. Luminosity of the force-free monopole rotator in flat space–time and in the slow rotation approximation with $R/r_L = \{0.01, 0.02, 0.05, 0.1, 0.2, 0.5\}$ and normalized to L_{dip}^{vac}. The different approximations are given in the legend and compared to the point dipole expectations $n = 3$, red line.

can be checked in Fig. 17. However we notice a decrease in the Poynting flux. This is due to the presence of the equatorial current sheet, forming a discontinuity that needs to be controlled by a filtering technique. This explains the dissipation of energy. The braking indexes for the Newtonian and GR split monopole solutions are compared and equal respectively to $n = 3.001$ and $n = 2.992$, obtained from fitting the absolute Poynting flux in Fig. 18 to a power law in R/r_L. The angular dependence of the Poynting flux for the force-free split monopole normalized to its total luminosity is equal to $l_{mono}^{vac}(\vartheta)$ and represented in Fig. 19. Because of the presence of a current sheet in the equatorial plane, the series expansion has trouble to adjust to such a discontinuity and the Gibbs phenomenon appears. This effect renders the convergence to the true solution very difficult as the error does only decrease linearly with the number of discretization points N_ϑ in the colatitude. In order to see the effect of the resolution on the accuracy of the luminosity, we looked at the convergence of the Poynting flux depending on the grid resolution in ϑ as shown in Fig. 20. Although the presence of the discontinuity, the Poynting flux converges to a constant value with only $N_\vartheta = 32$. The magnetic topology is not well represented along the equatorial plane but the global dynamics of the radiated power is still satisfactory.
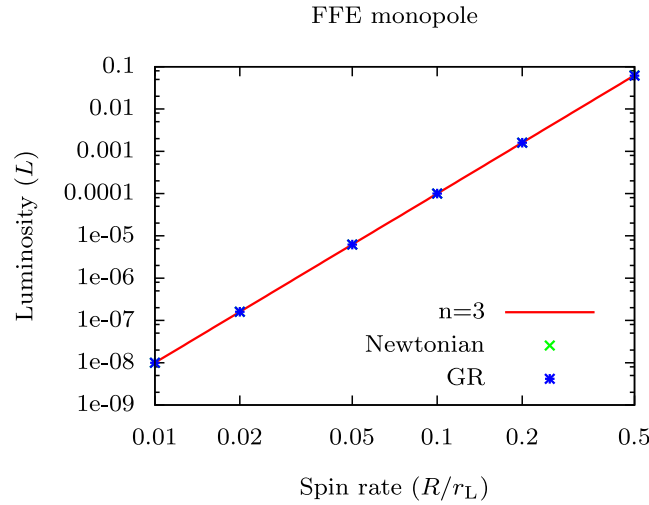
FFE monopole

Figure 13. Absolute Poynting flux of the force-free monopole. The different approximations are green crosses for Newtonian and blue stars for GR and compared to the point dipole expectations $n = 3$ in red.
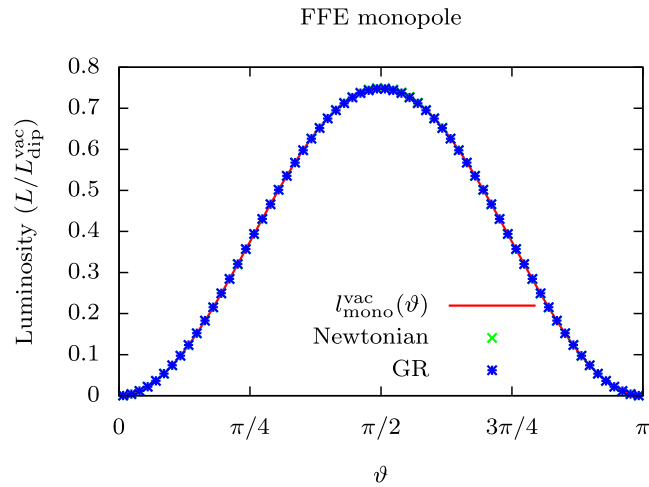
FFE monopole

Figure 14. Angular dependence of the Poynting flux for the force-free monopole in flat space–time, green crosses and in the slow rotation approximation, blue stars, with $R/r_{\mathrm{L}} = 0.2$. The fit to $\sin^2 \vartheta$ is shown in red.
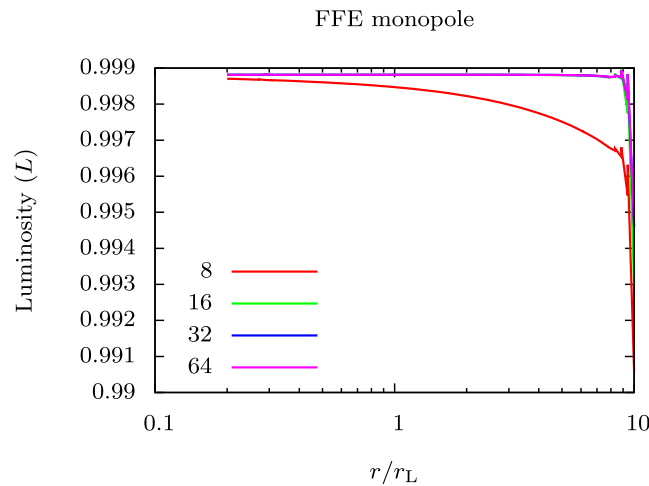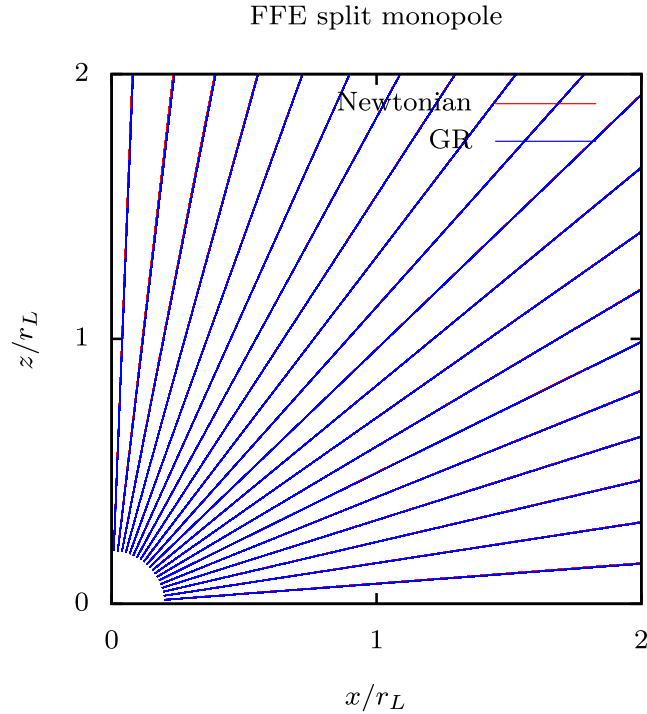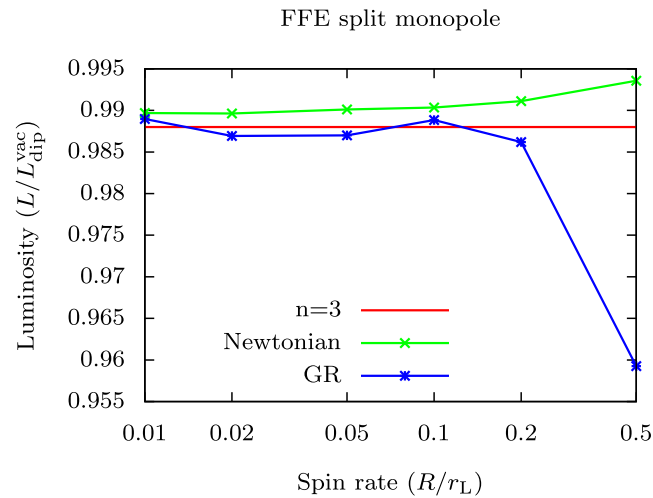
FFE monopole

Figure 15. Luminosity of the force-free monopole in the slow rotation approximation with $R/r_{\mathrm{L}} = 0.2$ and for different numerical resolutions $N_\vartheta = \{8, 16, 32, 64\}$ as given in the legend.

FFE split monopole

Figure 16. Meridional field lines for the force-free split monopole in flat space–time, red line, and in the slow rotation approximation, blue line, with $R/r_L = 0.2$.

FFE split monopole

Figure 17. Luminosity of the force-free split monopole in flat space–time, red line and in the slow rotation approximation, blue line, with $R/r_L = \{0.01, 0.02, 0.05, 0.1, 0.2, 0.5\}$. The different approximations are shown in green for Newtonian and blue in GR and compared to the point dipole expectations $n = 3$ in red.

5.3 Dipole

To finish this discussion, we summarize the new results about the rotating dipolar magnetosphere in the two limiting cases of an aligned and a perpendicular rotator. The main results of the simulations are the Poynting fluxes compared with respect to the Newtonian and GR geometry. Finally, we will show an example of dependence with respect to the obliquity.

In order to emphasize the discrepancies between Newtonian gravity and general relativity, in this last section, we normalize the Poynting flux with respect to the aligned force-free rotator in flat space–time given by

$$L_{dip}^{FFE} = \frac{3}{2} L_{dip}^{vac} \tag{48}$$

therefore better assessing the differences between both approximations.
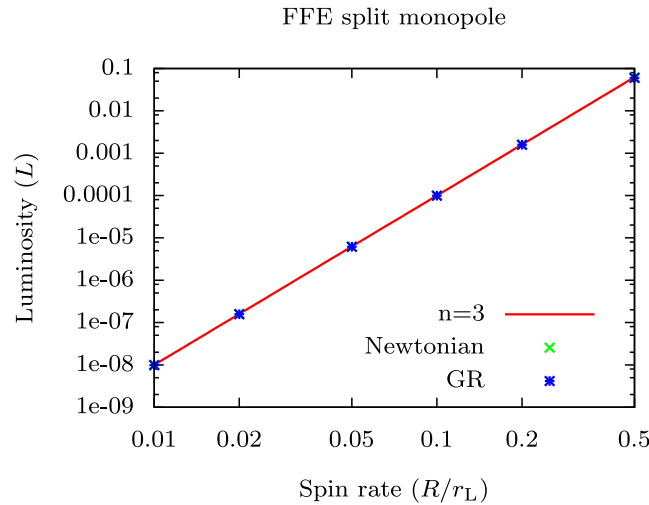
FFE split monopole

Figure 18. Absolute Poynting flux of the force-free split monopole. The different approximations are marked by symbols, green for Newtonian and blue for GR and compared to the point dipole expectations $n = 3$ in red.
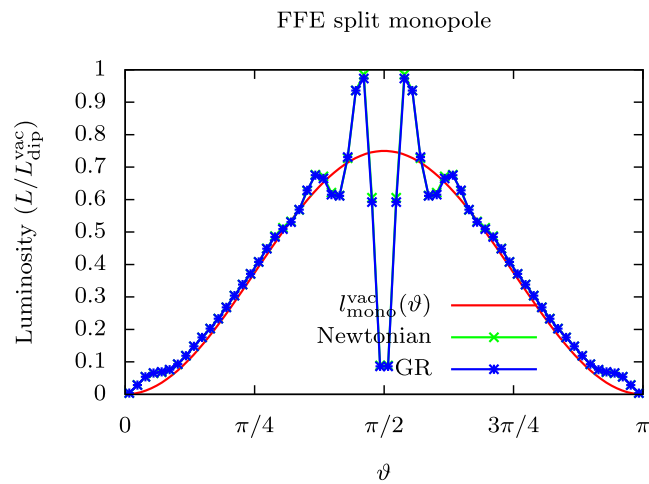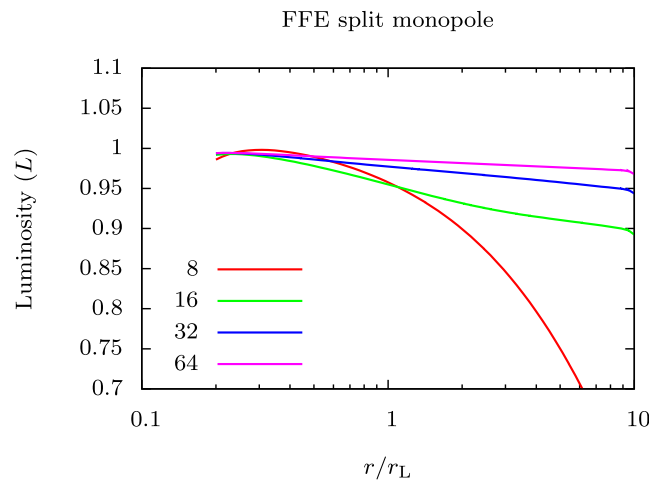
FFE split monopole

Figure 19. Angular dependence of the Poynting flux for the force-free split monopole in flat space–time, green crosses, and in the slow rotation approximation, blue stars, with $R/r_{\rm L} = 0.2$. The fit to $\sin^2\vartheta$ is shown in red.

FFE split monopole

Figure 20. Luminosity of the force-free split monopole in the slow rotation approximation with $R/r_{\rm L} = 0.2$ and for different numerical resolutions $N_\vartheta = \{8, 16, 32, 64\}$ as given in the legend.
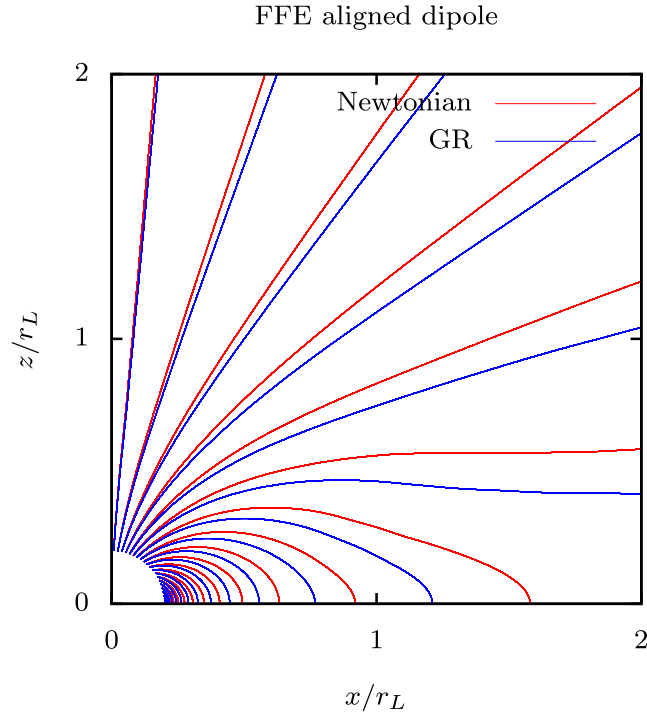
FFE aligned dipole

Figure 21. Meridional field lines for the force-free aligned dipole in flat space–time, red solid line and in the slow rotation approximation, blue solid line, with $R/r_L = 0.2$.
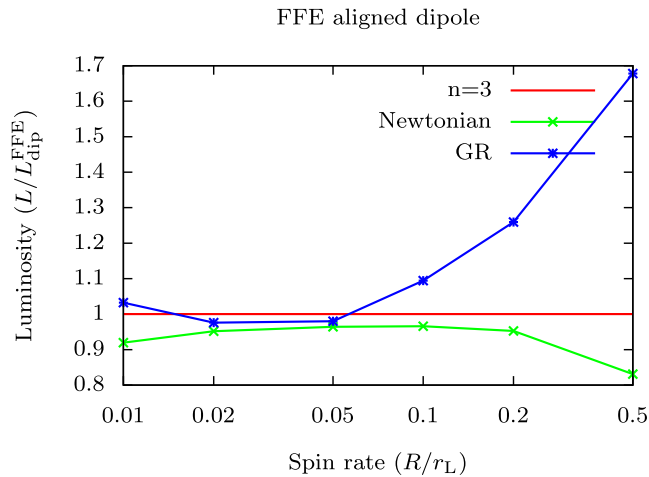
FFE aligned dipole

Figure 22. Poynting flux of the force-free aligned rotator for $R/r_L = \{0.01, 0.02, 0.05, 0.1, 0.2, 0.5\}$ and normalized to $L_{\rm dip}^{\rm FFE}$. The different approximations are shown in green for Newtonian and blue for GR and compared to the point dipole expectations $n = 3$ in red.

5.3.1 Aligned rotator

The aligned rotator has been investigated by many authors in flat space–time. Here we present new simulations including general relativity. First, we compare the magnetic field topology of the non-relativistic and the GR configurations. Examples of meridional field lines are shown in Fig. 21 for flat space–time in solid red line and for curved space–time in solid blue line for a rotation rate of $R/r_L = 0.2$. General relativity leads to a compression of the field lines towards the neutron star as already observed in the vacuum case. Qualitatively, the topology does not significantly changes in both cases but the size of the polar cap and the curvature of the field lines are nevertheless affected. Note that because of the unavoidable numerical resistivity, some magnetic field lines still close outside the light cylinder. The Poynting fluxes corresponding to the aligned rotator for several spin parameters $R/r_L = \{0.01, 0.02, 0.05, 0.1, 0.2, 0.5\}$ are described in Fig. 22. The current state of our code is pushed to its limit for very slow rotators with $R/r_L \lesssim 0.02$ because the size of the polar caps become very small, requiring higher resolutions, thus smaller radial grids and much smaller time steps. The computation time becomes prohibitive and we were unable to perform high resolution simulations within a reasonable CPU time. Nevertheless, let us have a look at the braking indexes for the Newtonian and GR aligned dipole. They are respectively $n = 2.97$ and $n = 3.12$, obtained from the fit shown in Fig. 23 for the absolute Poynting flux. The
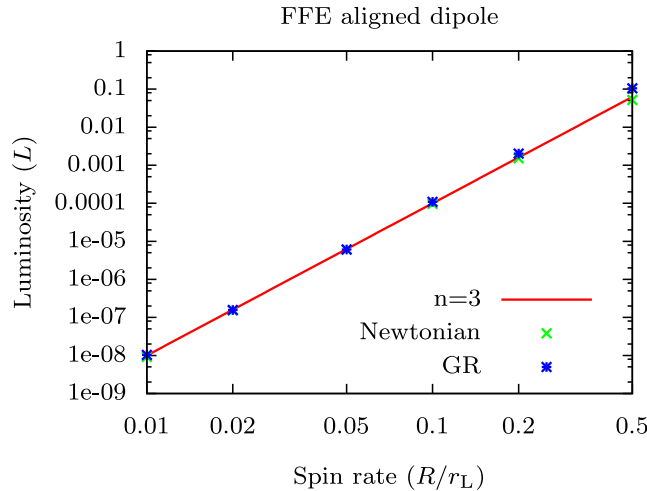
FFE aligned dipole

Figure 23. Absolute Poynting flux of the force-free aligned dipole rotator. The different approximations are marked by symbols, green for Newtonian and blue for GR and compared to the point dipole expectations $n = 3$ in red.
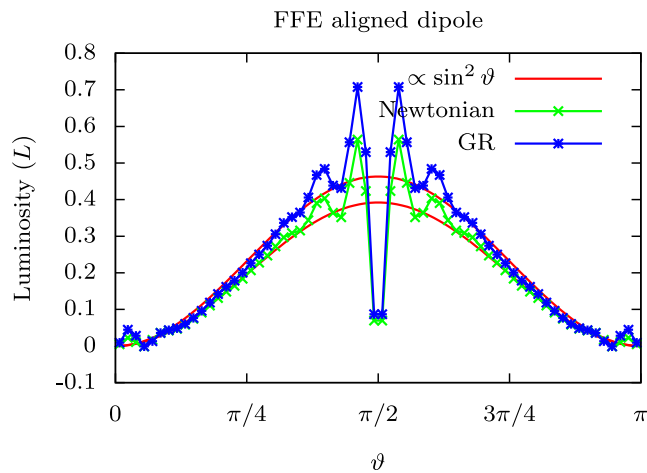
FFE aligned dipole

Figure 24. Angular dependence of the Poynting flux for the FFE aligned dipole in flat space–time, green line, and in the slow rotation approximation, blue line, with $R/r_{\rm L} = 0.2$. The fit to $\sin^2 \vartheta$ is shown in red.

angular dependence of the Poynting flux for the aligned dipole is depicted in Fig. 24. As for the split monopole, the presence of a current sheet in the equatorial plane renders the convergence difficult in this region. Nevertheless, elsewhere the solution is satisfactory. The variation of the Poynting flux with the colatitude ϑ has already been reported by Tchekhovskoy et al. (2013) for 3D MHD simulations. Moreover Tchekhovskoy, Philippov & Spitkovsky (2015) looked at some analytical expressions summarizing the bunch of results obtained from MHD and force-free simulations of an oblique rotator. Our plots are in good qualitative agreements with their findings. Dissipation in the equatorial current sheet prevents us to see an appreciable deviation from the monopole angular pattern as for instance claimed by these authors or by Timokhin (2006). In order to see the effect of the resolution on the accuracy of the luminosity, we looked at the convergence of the Poynting flux depending on the grid resolution in ϑ as shown in Fig. 25. Dissipation is reduced when the number of points is increased as expected. A reasonable number of grid points $N_\vartheta = 32$ or $N_\vartheta = 64$ is sufficient to obtain good accuracy inside the light cylinder. Nevertheless, outside we always get dissipation due to the presence of the current sheet in the equatorial plane. Our results seem a bit more dissipative than those obtained by the spectral code of Parfrey et al. (2012). This is mostly due to the coarser grid at the outer edge (remind the geometric series increase in the radial size of the cells) and the lower number of discretization points in the colatitude.

The increase in total luminosity can in part be explained by the increase in the transverse magnetic field in the vicinity of the light cylinder as was already discussed for the vacuum perpendicular rotator in the previous section. This is shown in Fig. 26 where in solid green curve we see the increase in luminosity induced by the curved space–time and the possible explanation in solid blue line in terms of transverse field at the light cylinder.

Comparing our results with Ruiz et al. (2014), we found a small discrepancy between their enhancement of the spin-down luminosity and our results. In their units, our compactness Ξ corresponds to their compaction $C = \Xi/2 = R_{\rm s}/(2\,R) = 0.25$ and the rotation rate of the neutron star is $\bar\Omega = R/r_{\rm L}$. In the GR case, we always obtain spin-down luminosities that are higher than the values they get. For $\bar\Omega = R/r_{\rm L} = 0.1$ the enhancement is about 10–15 per cent in our simulations and in Ruiz et al. (2014) results but for larger spin rate, for instance $\bar\Omega = R/r_{\rm L} = 0.2$
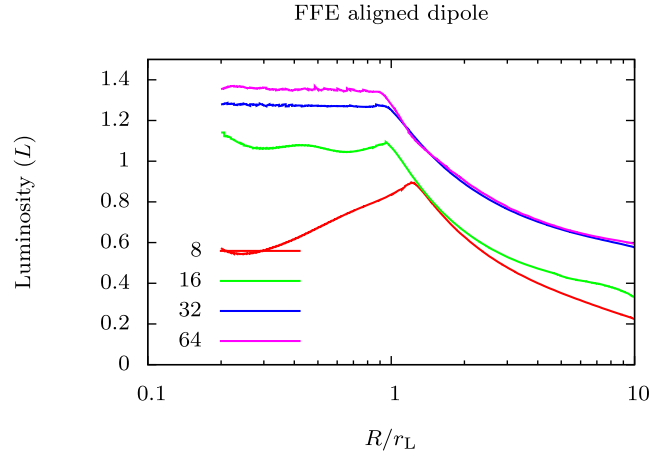
FFE aligned dipole

Figure 25. Luminosity of the force-free aligned dipole in the slow rotation approximation with $R/r_L = 0.2$ and for different numerical resolutions $N_\vartheta = \{8, 16, 32, 64\}$ as given in the legend.
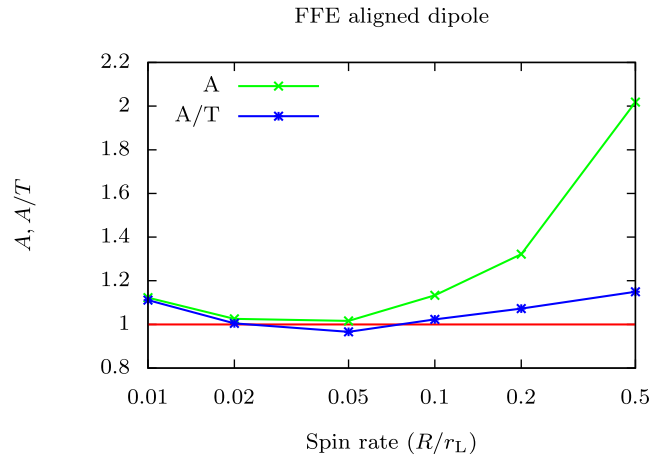
FFE aligned dipole

Figure 26. Comparison of the increase in total luminosity as obtained by the simulation for the GR case, solid green line, and as predicted by the increase in the transverse magnetic field, solid blue line. For reference the $L = 1$ line is shown in red.

we get about 30 per cent whereas they got 17 per cent. The deviation is even more pronounced for spin rates $\bar{\Omega} = R/r_L = 0.5$ (which are however unrealistic according to observations). However as these authors claimed, they expect 'stiffer equations of state and more rapidly rotating neutron stars lead to even larger enhancements'. Therefore the exact spin-down value depends on the equation of state used for the polytrope. In our case, we did not solve for the electromagnetic field inside the star so we must interpret the difference in enhancement by an effect from the boundary conditions imposed on the stellar surface. We fixed them to the exact GR non-rotating dipole for the inside solution whereas they computed it from a prescription for the stellar structure. In our case, the slow rotation approximation becomes questionable for $R/r_L = 0.5$. Indeed, at this spin rate the ratio between kinetic energy $T = I\Omega^2/2$ and gravitational binding energy $W = -3\,G\,M^2/(5\,R)$ for a homogeneous sphere of radius R given by

$$\frac{T}{|W|} = \frac{2}{3}\frac{R}{R_s}\left(\frac{R}{r_L}\right)^2 \tag{49}$$

is about 0.33, far from the $T \ll |W|$ condition. Thus rotational effect cannot be ignored for an accurate description of the neutron star shape and the results we found should not be taken to precisely.

5.3.2 Orthogonal rotator

Investigations of the orthogonal rotator follow the same line as the aligned case. Examples of equatorial field lines are shown in Fig. 27 for flat space–time in red and for curved space–time in blue, for a rotation rate of $R/r_L = 0.2$. The Poynting fluxes corresponding to the perpendicular rotator for several spin parameters $R/r_L = \{0.01, 0.02, 0.05, 0.1, 0.2, 0.5\}$ are described in Fig. 28. The braking indexes for the Newtonian and GR perpendicular dipole are respectively $n = 3.04$ and $n = 3.19$, obtained from the fits shown in Fig. 29. The angular dependence of the Poynting flux is depicted in Fig. 30. Contrary to the split monopole or aligned dipole, the current sheet in the equatorial plane has disappeared thus improving the convergence in the whole computational domain. We found that the flux behaves like $L(\vartheta) \propto \sin^4 \vartheta$
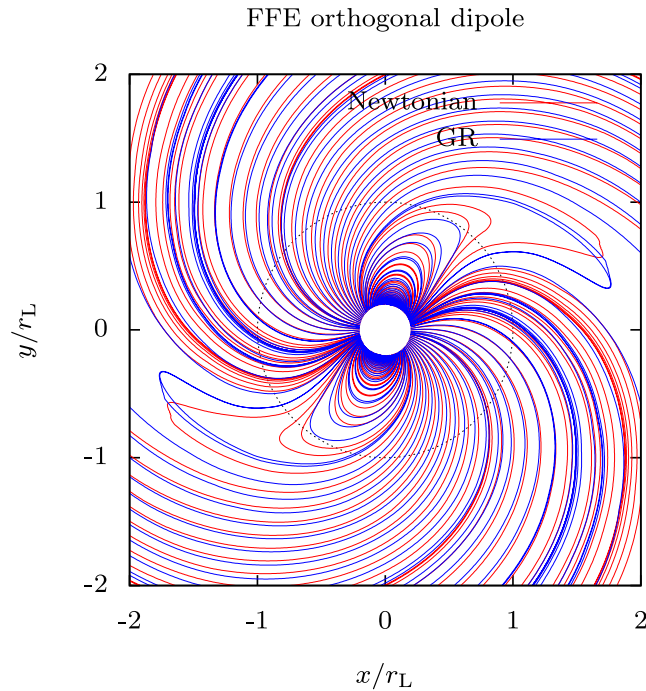
FFE orthogonal dipole

Figure 27. Equatorial field lines for the force-free perpendicular dipole in flat space–time, red solid line, and in the slow rotation approximation, blue solid line, with $R/r_L = 0.2$.
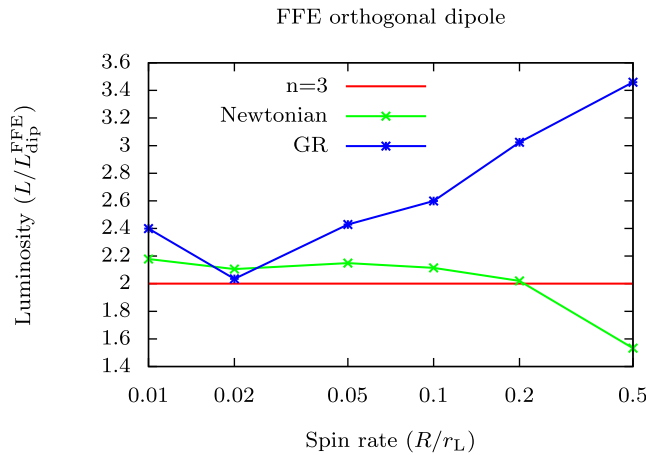

Figure 28. Poynting flux of the force-free orthogonal rotator normalized to L_{dip}^{FFE} and for $R/r_L = \{0.01, 0.02, 0.05, 0.1, 0.2, 0.5\}$. The different approximations are marked by symbols, green for Newtonian and blue for GR, and compared to the point dipole expectations $n = 3$, red line.

to good accuracy. Such simple fit to the luminosity was also proposed by Tchekhovskoy et al. (2013). The increase in total luminosity can in part be explained by the increase in the transverse magnetic field in the vicinity of the light cylinder as shown in Fig. 31.

5.3.3 Oblique rotator

To conclude, we performed a set of simulations for oblique rotators in the case $R/r_L = \{0.1, 0.2, 0.5\}$ and for obliquities $\chi = \{0°, 15°, 30°, 45°, 60°, 75°, 90°\}$ to check the dependence of the spin-down luminosity on the geometry in the force-free limit. The results are summarized in Fig. 32. All the curves can be fitted with an expression like

$$\frac{L}{L_{dip}^{FFE}} = a + b \sin^2 \chi \tag{50}$$

where a and b are constants. This behaviour is reminiscent of the vacuum dipole rotator in flat space–time. Best fits parameters for a and b are given in Table 2. As a general trend, curvature of space–time increases the overall Poynting flux. The coefficient a is not constant and approximately equal to unity as claimed in the simulations done by Philippov et al. (2014). We found a small decrease with respect to R/r_L consistent with the vacuum oblique rotator.
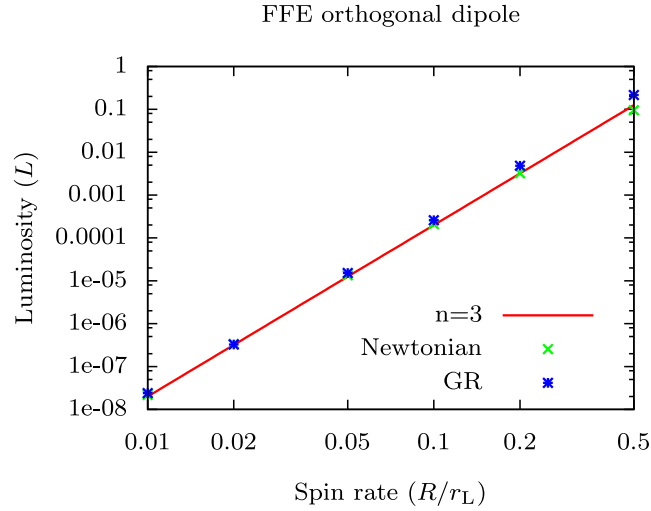
FFE orthogonal dipole

Figure 29. Absolute Poynting flux of the force-free orthogonal rotator. The different approximations are marked by symbols, green for Newtonian and blue for GR. They are compared to the point dipole expectations $n = 3$, red line.
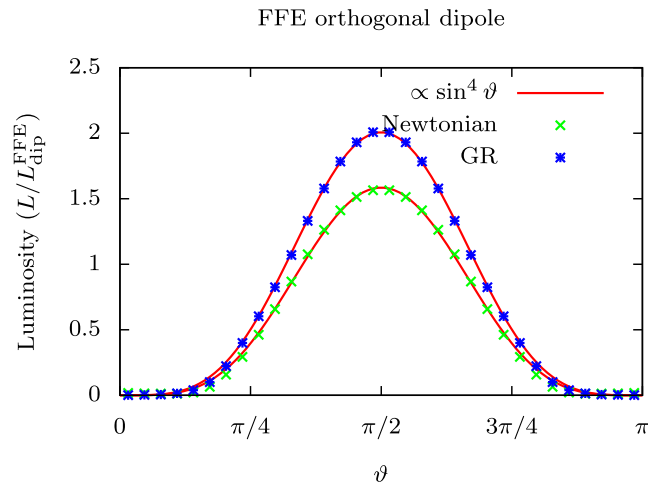
FFE orthogonal dipole

Figure 30. Angular dependence of the Poynting flux for the FFE orthogonal dipole in flat space–time, in green, and in the slow rotation approximation, in blue, with $R/r_L = 0.2$. A fit to $\sin^4 \vartheta$ is proposed in red.
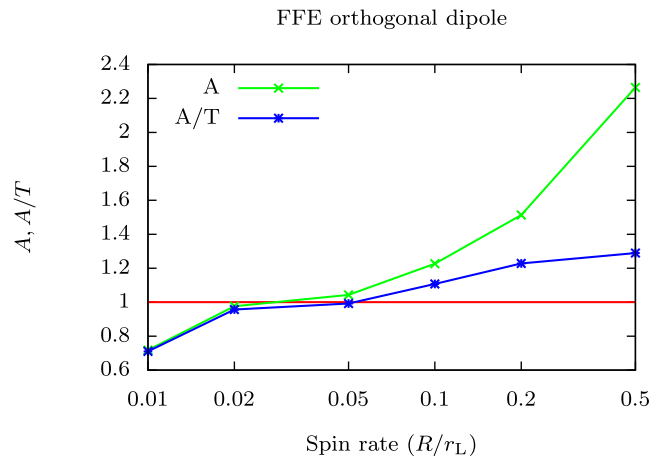
FFE orthogonal dipole

Figure 31. Comparison of the increase in total luminosity as obtained by the simulation, green line, and as predicted by the increase in the transverse magnetic field, blue line. For reference the $L = 1$ line is shown in red.
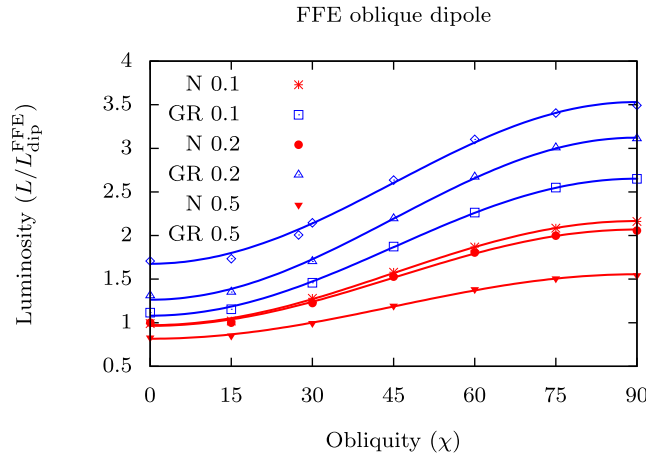
FFE oblique dipole

Figure 32. Poynting flux of the force-free oblique rotator for different obliquities χ and normalized to $L_{\mathrm{dip}}^{\mathrm{FFE}}$. Points are taken from the simulations and the solid lines are the best fits with $R/r_{\mathrm{L}} = \{0.1, 0.2, 0.5\}$. Red corresponds to Newtonian approximation (N) and blue to general relativity (GR).

Table 2. Best-fitting parameters a/b for the Poynting flux $L(\chi)/L_{\mathrm{dip}}^{\mathrm{FFE}} = a + b \sin^2 \chi$ of the FFE dipole rotator in Newtonian and GR cases.

R/r_{L}	Newtonian	GR
0.1	0.972/1.193	1.080/1.570
0.2	0.847/1.184	0.946/2.094
0.5	0.818/0.737	1.650/1.888

6 CONCLUSIONS

GR effects are important to understand the electrodynamical processes in the vicinity of neutron stars. This was already known in the case of a vacuum rotator for which the Poynting flux increases monotonically with increasing curvature and frame-dragging effects. These conclusions remain true for a force-free pulsar magnetosphere. The increase in spin-down luminosity can reach a factor up to 2 depending on the neutron star period, through the ratio R/r_{L}. The overall effect will be a change in the estimate of the surface dipolar magnetic field by several tenth of percents compared to flat space–time expectations. For the oblique rotator, we retrieve the law $L(\chi)/L_{\mathrm{dip}}^{\mathrm{FFE}} = a + b \sin^2 \chi$ for the Poynting flux, reminiscent of the Newtonian vacuum dipole except for slight changes in the constants a and b (a vanishing in vacuum). We were also able to investigate slow rotators with ratio R/r_{L} as small as 0.01. This helped us to compute the braking index n in vacuum and in the force-free limit. We found values always close to the fiducial braking index of $n = 3$.

Although force-free magnetospheres represent a useful first step to describe the global structure of relativistic plasmas evolving in the electromagnetic field of neutron stars, they do not furnish any information about the sites where particle acceleration and therefore radiation is supposed to occur. A good compromise between full PIC or MHD calculations and our simple force-free model, taking into account plasma inertia and finite temperature, would be to used a resistive prescription for the current density as already done by several authors. This extension is left for future work.

REFERENCES

Abdikamalov E. B., Ahmedov B. J., Miller J. C., 2009, MNRAS, 395, 443
Belyaev M. A., 2015, MNRAS, 449, 2759
Beskin V. S., 1990, Sov. Astron. Lett., 16, 286
Canuto C., Hussaini M., Quarteroni A., Zang T., 2006, Spectral Methods. Fundamentals in Single Domains. Springer-Verlag, Berlin
Canuto C., Hussaini M., Quarteroni A., Zang T., 2007, Spectral Methods. Evolution to Complex Geometries and Applications to Fluid Dynamics. Springer-Verlag, Berlin
Chen A. Y., Beloborodov A. M., 2014, ApJ, 795, L22
Cockburn B., Lin S.-Y., Shu C.-W., 1989, J. Comput. Phys., 84, 90

Gralla S. E., Jacobson T., 2014, MNRAS, 445, 2500
Gruzinov A., 2008, J. Cosmol. Astropart. Phys., 11, 2
Hesthaven J. S., Warburton T., 2008, Nodal Discontinuous Galerkin Methods: Algorithms, Analysis, and Applications. Springer-Verlag, Berlin
Kalapotharakos C., Contopoulos I., Kazanas D., 2012a, MNRAS, 420, 2793
Kalapotharakos C., Kazanas D., Harding A., Contopoulos I., 2012b, ApJ, 749, 2
Kim H., Lee H. M., Lee C. H., Lee H. K., 2005, MNRAS, 358, 998
Komissarov S. S., 2002, MNRAS, 336, 759
Komissarov S. S., 2004, MNRAS, 350, 427
Komissarov S. S., 2006, MNRAS, 367, 19
Krause-Polstorff J., Michel F. C., 1985, MNRAS, 213, 43
Krivodonova L., 2007, J. Comput. Phys., 226, 879
Li J., Spitkovsky A., Tchekhovskoy A., 2012, ApJ, 746, 60
McDonald J., Shearer A., 2009, ApJ, 690, 13
McKinney J. C., 2006, MNRAS, 368, L30
Morozova V. S., Ahmedov B. J., Kagramanova V. G., 2008, ApJ, 684, 1359
Morozova V. S., Ahmedov B. J., Zanotti O., 2010, MNRAS, 408, 490
Muslimov A. G., Tsygan A. I., 1990, SvA, 34, 133
Palenzuela C., 2013, MNRAS, 431, 1853
Parfrey K., Beloborodov A. M., Hui L., 2012, MNRAS, 423, 1416
Paschalidis V., Shapiro S. L., 2013, Phys. Rev. D, 88, 104031
Pétri J., 2012, MNRAS, 424, 605
Pétri J., 2013, MNRAS, 433, 986
Pétri J., 2014, MNRAS, 439, 1071
Pétri J., 2015a, MNRAS, 447, 3170
Pétri J., 2015b, MNRAS, 450, 714
Pétri J., Heyvaerts J., Bonazzola S., 2002, A&A, 384, 414
Philippov A. A., Spitkovsky A., 2014, ApJ, 785, L33
Philippov A., Tchekhovskoy A., Li J. G., 2014, MNRAS, 441, 1879
Philippov A. A., Spitkovsky A., Cerutti B., 2015, ApJ, 801, L19
Pili A. G., Bucciantini N., Del Zanna L., 2015, MNRAS, 447, 2821
Rezzolla L., Ahmedov B. J., 2004, MNRAS, 352, 1161
Ruiz M., Paschalidis V., Shapiro S. L., 2014, Phys. Rev. D, 89, 084045
Spitkovsky A., 2006, ApJ, 648, L51
Takamori Y., Okawa H., Takamoto M., Suwa Y., 2014, PASJ, 66, 25
Tchekhovskoy A., Spitkovsky A., Li J. G., 2013, MNRAS, 435, L1
Tchekhovskoy A., Philippov A., Spitkovsky A., 2015, preprint (arXiv:1503.01467)
Timokhin A. N., 2006, MNRAS, 368, 1055
Toro E. F., 2009, Riemann Solvers And Numerical Methods for Fluid Dynamics. Springer-Verlag, Berlin
Umizaki M., Shibata S., 2010, PASJ, 62, 131
Wada T., Shibata S., 2007, MNRAS, 376, 1460
Wada T., Shibata S., 2011, MNRAS, 418, 612
Yuki S., Shibata S., 2012, PASJ, 64, 43

This paper has been typeset from a TEX/LATEX file prepared by the author.